NASA/TM-20205001972

Comparison of Compressive Stress-Strain Responses at High Temperatures for Representative Single Crystal and Polycrystal Superalloys

T.P. Gabb, J. Telesman, and A.J. Ring
Glenn Research Center, Cleveland, Ohio

I.E. Locci
The University of Toledo, Toledo, Ohio

C.A. Kantzos and T.M. Smith
Glenn Research Center, Cleveland, Ohio

R.J. Pawlik
HX5 Sierra, LLC, Fort Walton Beach, Florida

L.J. Evans
Glenn Research Center, Cleveland, Ohio

June 2020

NASA STI Program . . . in Profile

Since its founding, NASA has been dedicated to the advancement of aeronautics and space science. The NASA Scientific and Technical Information (STI) Program plays a key part in helping NASA maintain this important role.

The NASA STI Program operates under the auspices of the Agency Chief Information Officer. It collects, organizes, provides for archiving, and disseminates NASA's STI. The NASA STI Program provides access to the NASA Technical Report Server—Registered (NTRS Reg) and NASA Technical Report Server—Public (NTRS) thus providing one of the largest collections of aeronautical and space science STI in the world. Results are published in both non-NASA channels and by NASA in the NASA STI Report Series, which includes the following report types:

- TECHNICAL PUBLICATION. Reports of completed research or a major significant phase of research that present the results of NASA programs and include extensive data or theoretical analysis. Includes compilations of significant scientific and technical data and information deemed to be of continuing reference value. NASA counter-part of peer-reviewed formal professional papers, but has less stringent limitations on manuscript length and extent of graphic presentations.

- TECHNICAL MEMORANDUM. Scientific and technical findings that are preliminary or of specialized interest, e.g., "quick-release" reports, working papers, and bibliographies that contain minimal annotation. Does not contain extensive analysis.

- CONTRACTOR REPORT. Scientific and technical findings by NASA-sponsored contractors and grantees.

- CONFERENCE PUBLICATION. Collected papers from scientific and technical conferences, symposia, seminars, or other meetings sponsored or co-sponsored by NASA.

- SPECIAL PUBLICATION. Scientific, technical, or historical information from NASA programs, projects, and missions, often concerned with subjects having substantial public interest.

- TECHNICAL TRANSLATION. English-language translations of foreign scientific and technical material pertinent to NASA's mission.

For more information about the NASA STI program, see the following:

- Access the NASA STI program home page at http://www.sti.nasa.gov

- E-mail your question to help@sti.nasa.gov

- Fax your question to the NASA STI Information Desk at 757-864-6500

- Telephone the NASA STI Information Desk at 757-864-9658

- Write to:
  NASA STI Program
  Mail Stop 148
  NASA Langley Research Center
  Hampton, VA 23681-2199

NASA/TM-20205001972

Comparison of Compressive Stress-Strain Responses at High Temperatures for Representative Single Crystal and Polycrystal Superalloys

T.P. Gabb, J. Telesman, and A.J. Ring
Glenn Research Center, Cleveland, Ohio

I.E. Locci
The University of Toledo, Toledo, Ohio

C.A. Kantzos and T.M. Smith
Glenn Research Center, Cleveland, Ohio

R.J. Pawlik
HX5 Sierra, LLC, Fort Walton Beach, Florida

L.J. Evans
Glenn Research Center, Cleveland, Ohio

National Aeronautics and
Space Administration

Glenn Research Center
Cleveland, Ohio 44135

June 2020

Acknowledgments

The authors acknowledge the support of NASA's Aeronautics Research Mission Directorate (ARMD) –Advanced Air Transport Technology (AATT) Project Office. Joy Buehler of Vantage Partners, LLC is acknowledged for careful metallographic preparation of all sectioned test materials in the metallography lab of the Analytical Sciences Group at NASA Glenn Research Center, and Rick Rogers of NASA Glenn Research Center is acknowledged for Laue x-ray verifications of the crystallographic orientations of the SC-180 single crystal bars in the x-ray diffraction lab of the Analytical Sciences Group. Peter Bonacuse of NASA Glenn Research Center is acknowledged for carefully reviewing this manuscript.

This work was sponsored by the Advanced Air Vehicle Program
at the NASA Glenn Research Center

Level of Review: This material has been technically reviewed by technical management.

Available from

NASA STI Program
Mail Stop 148
NASA Langley Research Center
Hampton, VA 23681-2199

National Technical Information Service
5285 Port Royal Road
Springfield, VA 22161
703-605-6000

This report is available in electronic form at http://www.sti.nasa.gov/ and http://ntrs.nasa.gov/

Comparison of Compressive Stress-Strain Responses at High Temperatures for Representative Single Crystal and Polycrystal Superalloys

T.P. Gabb, J. Telesman, and A.J. Ring
National Aeronautics and Space Administration
Glenn Research Center
Cleveland, Ohio 44135

I.E. Locci
The University of Toledo
Toledo, Ohio 43606

C.A. Kantzos and T.M. Smith
National Aeronautics and Space Administration
Glenn Research Center
Cleveland, Ohio 44135

R.J. Pawlik
HX5 Sierra, LLC
Fort Walton Beach, Florida 32548

L.J. Evans
National Aeronautics and Space Administration
Glenn Research Center
Cleveland, Ohio 44135

Abstract

Polycrystalline disk superalloys and single crystal blade superalloys have divergent grain and precipitate microstructures but can each display reduced strength and increasing deformation for certain test conditions at high temperatures. To allow thermo-mechanical processes such as forging and rolling to be applied, favorable temperatures and strain rates must first be identified using compression testing. The objective of this study was to perform compression tests at high temperatures on a polycrystalline disk superalloy and a single crystal blade superalloy in order to compare their stress-strain responses for given test conditions and determine preferred conditions. It was determined that the conditions required for stable flow differed significantly between the polycrystalline and single crystal superalloys. The conditions leading to unstable flow were also identified for each alloy. The microstructural deformation modes for both stable and unstable flow are discussed.

Introduction

Polycrystalline turbine disk alloys contain moderate levels of strengthening refractory elements and about 45 to 55 percent of γ′ precipitates with relatively low γ′ solvus temperatures of 1100 to 1200 °C, to allow versatile thermomechanical processing necessary to produce high performance turbine disks

(Refs. 1 and 2). When processed to produce uniform microstructures with grain sizes of 10 to 60 μm in diameter, these alloys can exhibit good tensile strength, creep resistance, and fatigue resistance at temperatures up to 760 °C. In contrast, single crystal turbine airfoil superalloys have increased levels of strengthening refractory elements and about 65 to 70 percent of γ′ precipitates with higher γ′ solvus temperatures. When carefully cast as a single crystals grown in the [001] crystallographic orientation, which gives low elastic modulus and multiple favorable deformation systems, these alloys can provide superior creep and thermal fatigue resistance for potential airfoil applications at temperatures up to 1200 °C (Refs. 1 and 2).

Due to their strengthening γ′ precipitates, polycrystalline disk superalloys have high flow stress and are difficult to deform at low and intermediate temperatures. However, at high temperatures approaching their γ′ solvus temperatures, disk alloys can have reduced flow stress and support more extended deformation. This is largely attributed to the grain boundary sliding mechanism which becomes the dominant deformation mode at temperatures above 760 °C and can allow stable superplastic flow at temperatures above 900 °C (Refs. 3 and 4). Dynamic recrystallization can also occur in some deformation conditions (Refs. 5 and 6).

The same trends of reduced flow stress and extended inelastic deformation occur in single crystal superalloys, although for different reasons. The variations in γ′ contents and solvus temperatures, as well as grain size and anisotropic properties could have divergent effects on inelastic deformation for a fixed test condition applied to these two classes of superalloys. In single crystal airfoil superalloys, slip deformation by dislocations on {111} octahedral planes in <101> directions is usually reported at temperatures up to about 900 °C (Refs. 7 and 8). At higher temperatures and strain rates of at least 0.001 s^{-1}, slip by dislocations on {001} cube planes in <101> directions becomes more likely (Refs. 7 and 8). This usually includes shearing of the γ′ precipitates by pairs of associated dislocations (Ref. 9). At intermediate strain rates, time-dependent shearing of the γ′ precipitates by micro-twins (Refs. 10 and 11) or stacking faults can occur, while at slower strain rates dislocations can climb to by-pass the precipitates (Refs. 12 and 13).

Gas turbine engines can sometimes use both of these classes of superalloys in a single assembled rotating component, with a polycrystalline superalloy turbine disk holding single crystal superalloy turbine blades in a stage of the high pressure turbine (Refs. 1 and 2). For applications requiring increases in gas temperature and efficiency, it could be beneficial if the disk rim holding the blades were also made of a single crystal superalloy. This would require attachment of single crystal rim segments onto a polycrystalline disk (Ref. 14). Given their divergent compositions, grain boundary contents, and strengthening γ′ phase contents, consideration of attachment concepts would require an understanding of the stress-strain responses of these two classes of superalloys over a consistent range of input mechanical testing conditions. The emphasis of this study was to evaluate and contrast the effects of temperature and strain rate on a polycrystalline disk superalloy and a single crystal blade superalloy through the use of compression testing. The objective of the present study was to contrast the stress-strain responses of these divergent alloys and microstructures.

Material and Procedure

The tested compositions of the chosen single crystal superalloy SC-180 (Ref. 15) and polycrystalline disk superalloy LSHR (Refs. 4 and 14) are listed in Table I. The polycrystalline LSHR was produced by atomization of powder, hot compaction, extrusion, and isothermal forging of a pancake disk. Most specimen blanks were solution heat treated above the solvus of the γ′ precipitates at a “supersolvus” temperature 1171 °C for 2 h and air cooled at an average rate of 72 °C/min, and then aging heat treated at

TABLE I.—COMPOSITION IN WEIGHT PERCENT OF THE TESTED SUPERALLOYS

Alloy – wt.%	Al	B	C	Co	Cr	Fe	Hf	Mo	Ni	Nb	O	Re	Si	S	Ta	Ti	V	W	Y	Zr
LSHR	3.540	0.03	0.045	20.4	12.30	0.1	0.0	2.71	Bal.	1.49	0.02	----	0.012	0.001	1.520	3.45	0.01	4.28	<0.0005	0.049
SC-180	5.035	----	0.003	10	5.40	0.04	0.09	1.75	Bal.	----	----	3.065	0.040	0.001	8.725	0.99	----	5.00	----------	0.006

855 °C for 4 h plus 775 °C for 8 h. A small group of additional specimen blanks were prepared using a lower solution heat treatment temperature below the solvus of the γ′ precipitates at a "subsolvus" temperature of 1135 °C to produce finer grain size with some coarse, undissolved γ′ precipitates. Several of these fine grain specimens were given the same air cooling rate and subsequent aging heat treatment as for the supersolvus heat treated specimens. Other fine grain specimens were directly dropped from the furnace hot zone into water for a much faster cooling rate and given no aging heat treatment, to minimize the sizes of "cooling" γ′ precipitates reformed during this quench.

The single crystal SC-180 was obtained as cast single crystal bars grown within 8° of the [001] crystallographic direction. Some bars were given only the initial homogenization-solution heat treatment giving varied γ′ precipitate sizes. Additional bars were prepared using both the solution and aging heat treatments for SC-180, as described in Reference 15, to produce refined, more uniform γ′ precipitate sizes. For each alloy, right circular cylinder specimens having a diameter of 7 mm and length of 14 mm were extracted by electro-discharge machining and then low stress ground to final dimensions. The SC-180 specimens were all machined parallel to the centerline of single crystal bars which had been confirmed using Laue x-ray diffraction to be oriented within 8° of the [001] crystallographic growth direction.

Specimens were tested at three target temperatures of 1010, 1093, and 1177 °C with strain rates from 0.01 to 10 s^{-1}. These were tested at Dynamic Systems Inc. in a Gleeble 3800 Series 3 machine (Ref. 16) with the specimen enclosed in a chamber maintained at a vacuum of 10^{-3} torr. Direct resistance heating with an integrated closed-loop temperature control system was utilized to produce a consistent heating rate of 1 °C/s and then maintain the temperature during compression testing, with specimen temperature measured by a thermocouple spot-welded to the cylindrical surface midway between the top and bottom faces. After heating up, the compression test temperature was stabilized for 60 s, then tests were immediately commenced at the constant targeted strain rate while temperature was maintained. All tests were continued to an aim upset of 0.50 mm/mm, and target true strain of 0.70 mm/mm. However, several specimens of each alloy failed before reaching this point, as will be described in the results. After achieving maximum strain, all tests were cooled by elimination of heating power while maintained at zero load.

Tested LSHR and SC-180 specimens were metallographically prepared for examination on a longitudinal plane parallel to the loading direction. LSHR specimens were etched to highlight grain boundaries using Kallings reagent. Grain microstructures were evaluated in a Reichert MeF3 optical microscope with an Olympus DP72 digital camera and STREAM software, then electron back scattered diffraction (EBSD) analyses were performed in a Zeiss Auriga Focused Ion Beam/Scanning Electron Microscope (FIB/SEM) using an EDAX Hikari EBSD detector. Data collection and post-processing of the maps were done using the TSL OIM Data Collection 7 software. LSHR and SC-180 specimens were etched to highlight γ′ phase particles using 33 HCl-33 HNO_3 -33 H_2O-1HF. Precipitate microstructures were evaluated using Hitachi S4700 and Tescan MAIA3 field emission scanning electron microscopes. Fracture surfaces were evaluated in a JEOL 6100 scanning electron microscope.

Statistical evaluations of responses were performed using the JMP® 11 statistical software package (Ref. 17). Controlled variables V were expressed in standardized form *V'* using the equation:

$$V' = (V - V_{mid})/(0.5*(V_{max} - V_{min})) \quad (1)$$

This produced a range of values from –1 to +1 for each standardized variable of temperature (T') and common logarithm of strain rate ($log(d\varepsilon/dt)'$). Regression model equations were derived by comparing the results of both forward and reverse stepwise term selection, with a 95 percent probability of significance required for inclusion of a term. The expression of standardized variables is useful when comparing significant effects, as the relative effect on the response of each significant variable could then be assessed by directly comparing the magnitude of the coefficient for each variable (Ref. 17).

Results and Discussion

Starting Microstructures

The microstructures in prepared specimens of LSHR varied significantly with heat treatment, as shown in Figure 1. Supersolvus heat treated LSHR had a mean linear intercept grain size of 15 μm, while subsolvus heat treated LSHR had a grain size of 8 μm. Primary and secondary γ′ sizes are compared in Figure 2. The secondary γ′ precipitates of LSHR were finer than those for SC-180, as shown in Figure 2 to Figure 3. However, the primary γ′ particles in the subsolvus heat treated LSHR were larger (0.4 to 4.0 μm), and were estimated to provide negligible strengthening. Solution heat treated SC-180 had more

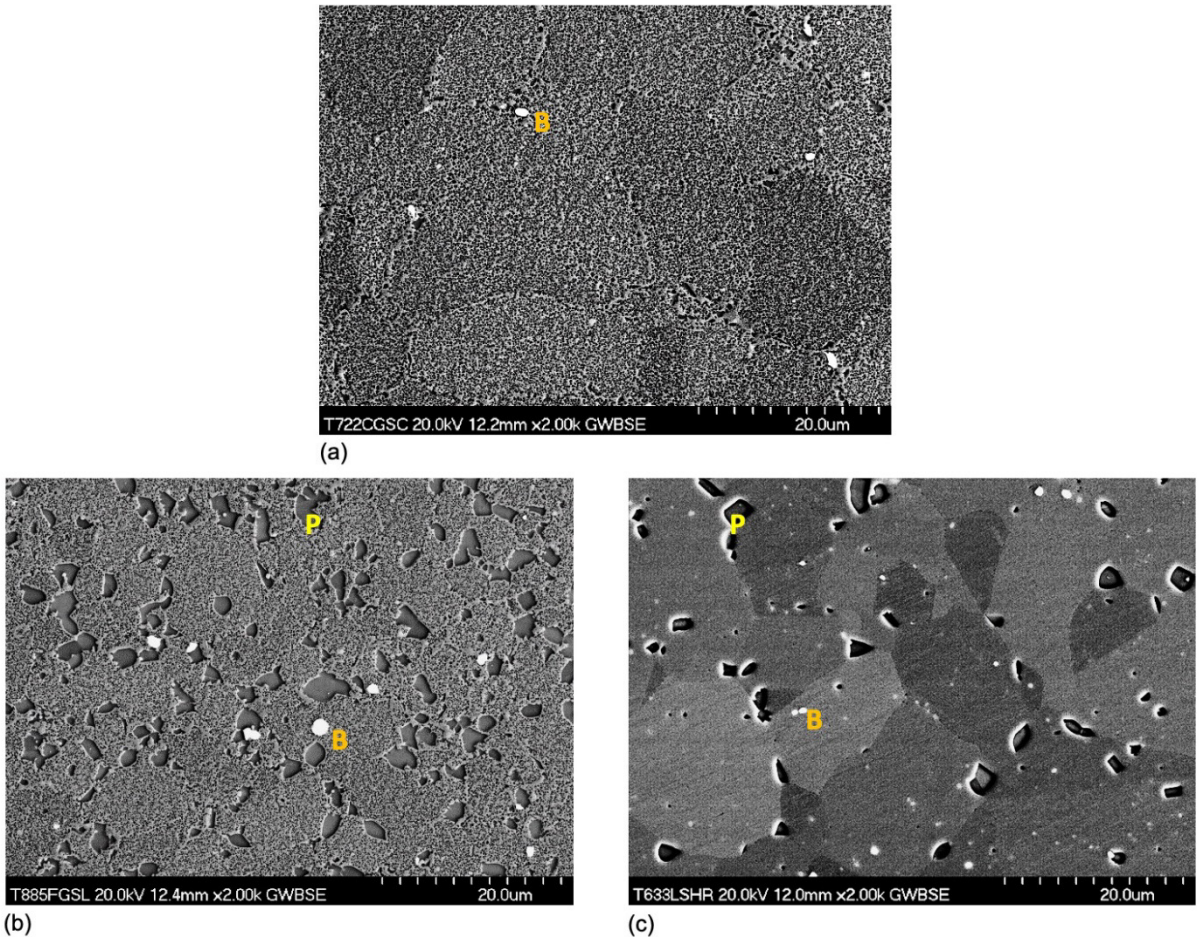

Figure 1.—Low magnification scanning electron microscope (SEM) images acquired using the backscattered electron (BSE) detector, for microstructures of: (a) “coarse grain” LSHR after 1171 °C-2h+slow cooled and aged, (b) “fine grain” LSHR after 1135 °C-2h+slow cooled and aged, (c) “fine grain” LSHR after 1135 °C-2h+water quenched. Large dark primary γ‘ particles (P) indicated for the fine grain materials. Smaller bright boride particles (B) indicated for all materials.

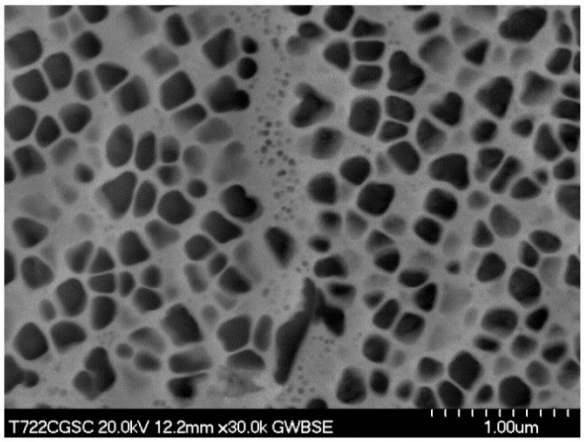

(a)

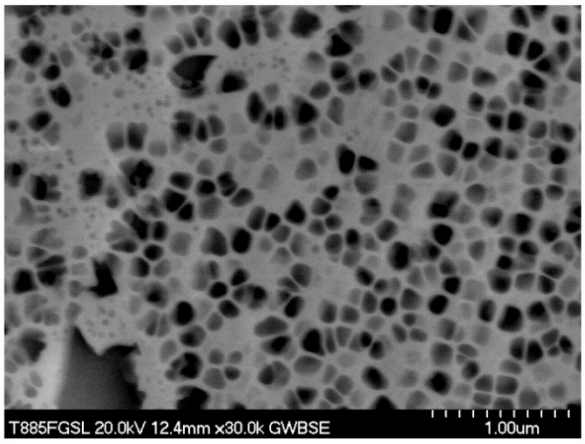

(b)

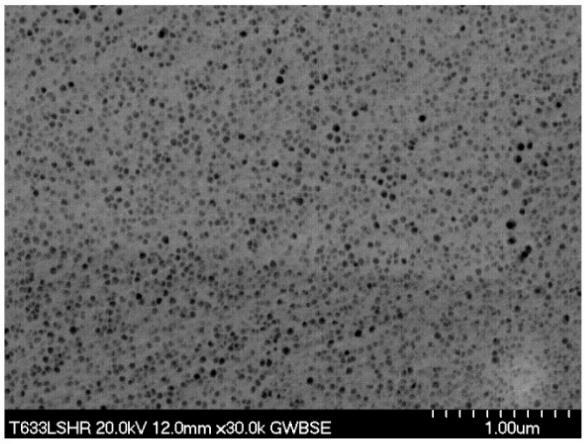

(c)

Figure 2.—High magnification scanning electron microscope BSE images of microstructures for: (a) LSHR after 1171 °C-2h+slow cooled and aged, (b) LSHR after 1135 °C-2h+slow cooled and aged, (c) LSHR after 1135 °C-2h+water quenched.

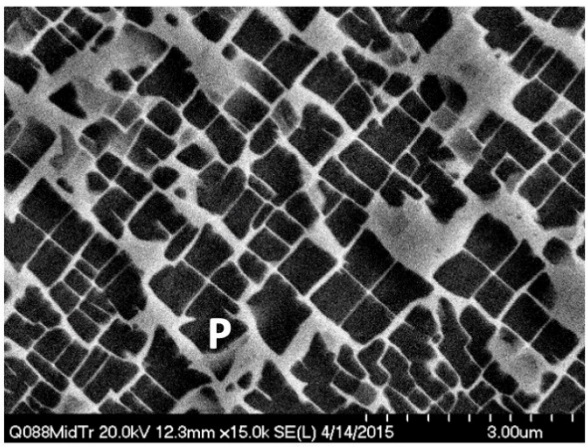

(a)

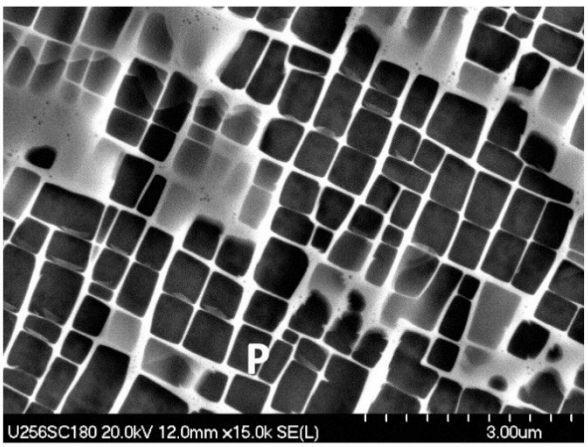

(b)

Figure 3.—High magnification scanning electron microscope images of SC-180 γ’ microstructures: (a) image acquired using the secondary electron (SE) detector after initial solution heat treatment, showing varied sizes of γ’ precipitates (P), (b) BSE image after subsequent solution heat treatments plus gas furnace quench and aging heat treatments, showing more uniform sizes of γ’ precipitates (Ref. 14).

varied secondary γ′ sizes than that for the fully heat treated SC-180, as shown in Figure 3. Tertiary γ′, with sizes less than 0.05 μm, were observed in all these material conditions but these particles would be expected to dissolve before reaching the test temperatures. Therefore, the tertiary γ′ precipitates were not quantified or compared among conditions.

Poly-Crystal Compression Response

Stress-Strain Response

True stress-strain curves are shown for all tests of coarse grain LSHR in Figure 4(a). Stress at a given strain clearly increased with increasing strain rate and decreased with increasing temperature. Yet, the shapes of these curves also changed with conditions, with unstable steep reductions in stress with increasing strain for some conditions. The unstable response was most severe at the highest test temperature near 1177 °C and at the highest strain rates of 1 to 10 s^{-1}. In these cases, the specimens attained a peak stress and then became very weak. The specimens sometimes even fractured into multiple pieces before attaining the target true strain of 0.70 mm/mm.

The unstable response observed near 1177 °C and high strain rates could be influenced by the starting grain microstructure and γ′ precipitates. To further explore this unstable response, additional specimens prepared with finer grain size and with finer secondary γ′ sizes as shown in Figure 1 and Figure 2 were also tested at a fast strain rate of 3 s^{-1} with varied test temperature. The resulting stress-strain curves are compared in Figure 4(b). The specimens with finer grain size still had unstable stress strain curves in tests at 1177 °C, but did not completely fail before reaching 0.70 mm/mm true strain. This modest improvement occurred both with the standard cooling rate combined with aging heat treatment, as well as with the very fast water quench combined with no aging heat treatment. However, starting grain size and heat treatment condition variations did not show a consistent influence on maximum stress attained in the limited number of tests performed here. Conversely, reducing test temperature to 1093 °C gave larger improvements in stability of stress-strain response at these high strain rates for both coarse grain and fine grain microstructure conditions, as well as increasing the maximum stress attained. This is illustrated more clearly in Figure 4(c), only presenting tests performed at a strain rate of 3 s^{-1}.

Due to changes in the shape of the stress-strain curves, the maximum stress generated during each test was selected for consistent comparisons of stress -bearing capabilities with respect to strain rate and temperature. Plots of maximum stress values are shown versus temperature and versus strain rate in Figure 5(a) and (b). Variations in maximum stress are evident with temperature and strain rate. Strain rate sensitivity (m) can be modeled by the relationship $\sigma = K(d\varepsilon/dt)^m$ (Ref. 18). A material is usually considered superplastic in deformation conditions where a strain rate sensitivity m of at least 0.3 is observed. This can be desirable for enabling material working operations such as forging and hot rolling (Ref. 18). The strain rate sensitivity m was evaluated by fitting linear regression equations to the log(Max stress) data as a function of log(strain rate) at constant temperature, according to the equation:

$$\log(\sigma) = \log K + m \log(d\varepsilon/dt) \tag{2}$$

The log(max stress) versus log(strain rate) response is shown in Figure 6 Here, the slope of the regressed line is the strain rate sensitivity (m) as shown for 1010 °C in blue and for 1177 °C in red. At each test temperature, LSHR had a strain rate sensitivity m that was below 0.3 for these test conditions, and hence did not show a true superplastic response. Prior work has shown that when not forged and heat treated, LSHR behaves superplastic in tests performed in this temperature range at slower strain rates - up to 0.1 s^{-1} (Ref. 4). As a consequence, it is apparent slow strain rates are necessary to encourage a superplastic response through grain boundary sliding.

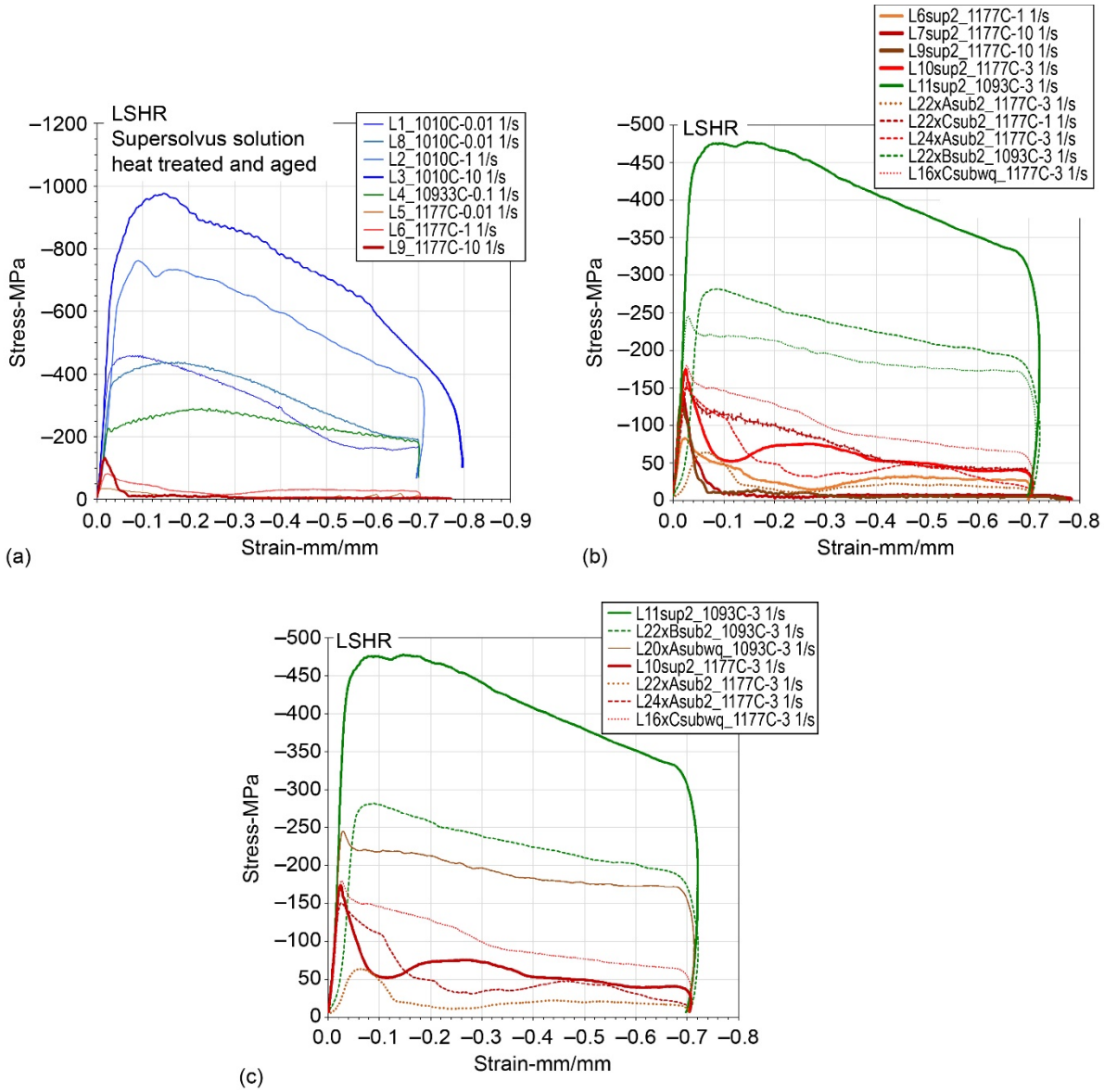

Figure 4.—LSHR true stress-true strain response for (a) all temperatures and varied strain rates, and (b) high strain rates with varied microstructures. (c) LSHR true stress-true strain response for tests at a strain rate of 3 s^{-1} with varied microstructures. Flow was not sustained well near 1177 °C (red curves).

Maximum stresses generated in tests performed at 3 s^{-1} on material with the fine grain heat treatment using the baseline cooling rate plus aging heat treatment and with fine grain as-water quenched heat treatment are also included in Figure 5 and Figure 6. No clear difference in maximum stresses was discernable for these specimens in the limited tests performed at 1093 and 1177 °C. Evidently, many of the finest γ′ precipitates are quickly dissolved when heating to 1093 or 1177 °C such that the differences in their sizes produced by the different heat treatments have negligible effects on maximum strength when tested at these temperatures.

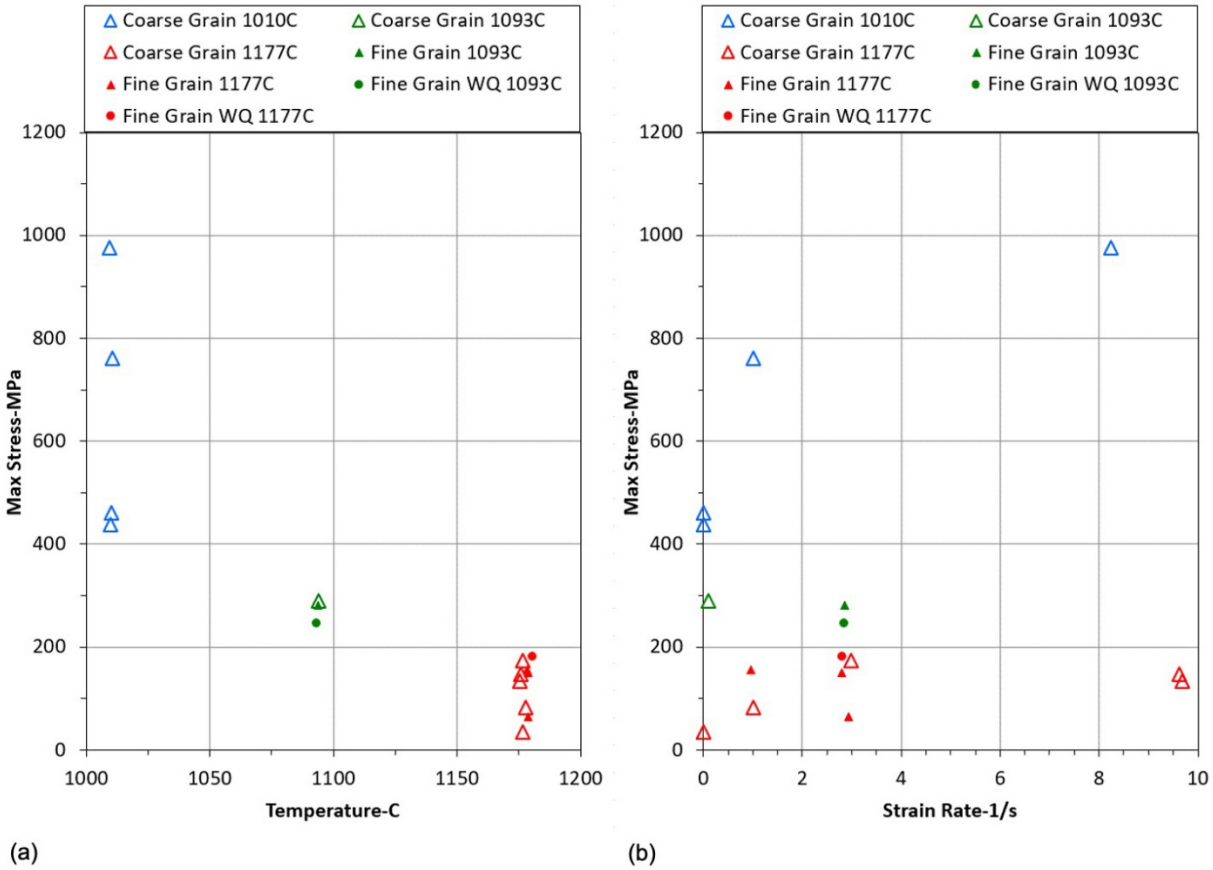

Figure 5.—Maximum stress response of LSHR versus: (a) temperature and (b) strain rate for fully heat treated coarse grain and fine grain materials shown in triangles, as well as as-water quenched fine grain material shown in circles. Grain size and heat treatment condition did not have a strong influence on maximum stress.

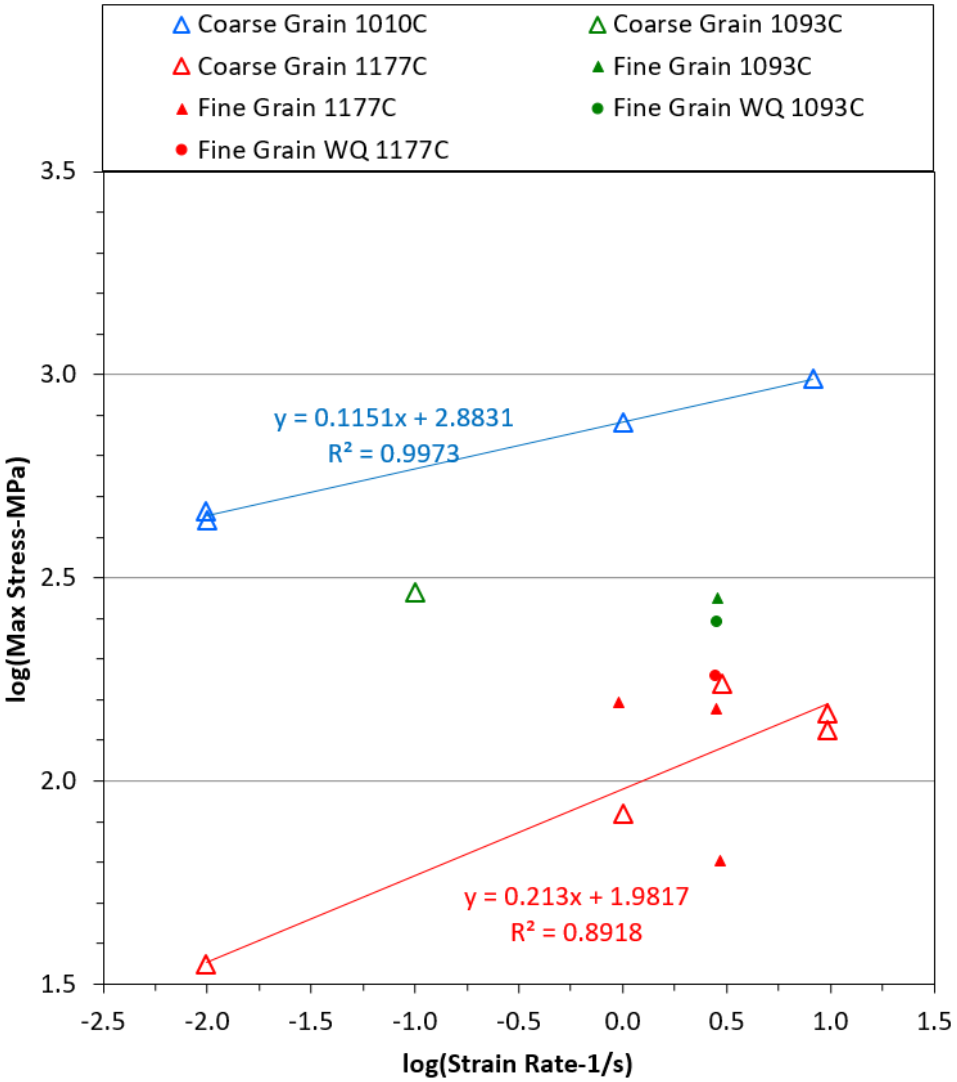

Figure 6.—Log(Maximum stress) versus log(strain rate) response of LSHR. The slopes of the regressed lines are the strain rate sensitivities m at 1010 °C (blue line) and 1177 °C (red line).

Deformation-Grain Microstructure Relationships

Macroscopic optical images of the deformed overall specimen cross sections observed for LSHR specimens after varied compression test conditions are compared in Figure 7. These images are arranged in rows of isotherms to highlight changes with increasing compression test temperature, and in columns of increasing strain rate. Severe cracking was observed in tests at the highest temperature of 1177 °C. Only minor cracks were observed at the side surfaces of specimens deformed at lower temperatures.

The typical grain structures observed for each tested condition are compared in the optical images of Figure 8. Linear intercept grain size measured from optical images is indicated for each test condition. Specimens tested near 1010 and 1094 °C showed deformed grains with decreased height in the compressive loading direction. Along most grain boundaries, finer features are observed that were not easily resolved in optical imaging of these etched specimens. Specimens tested near 1177 °C had more equiaxed grains with distinct, smooth grain boundaries, which had apparently formed by dynamic recrystallization during deformation at this temperature. Electron back-scattered diffraction images from

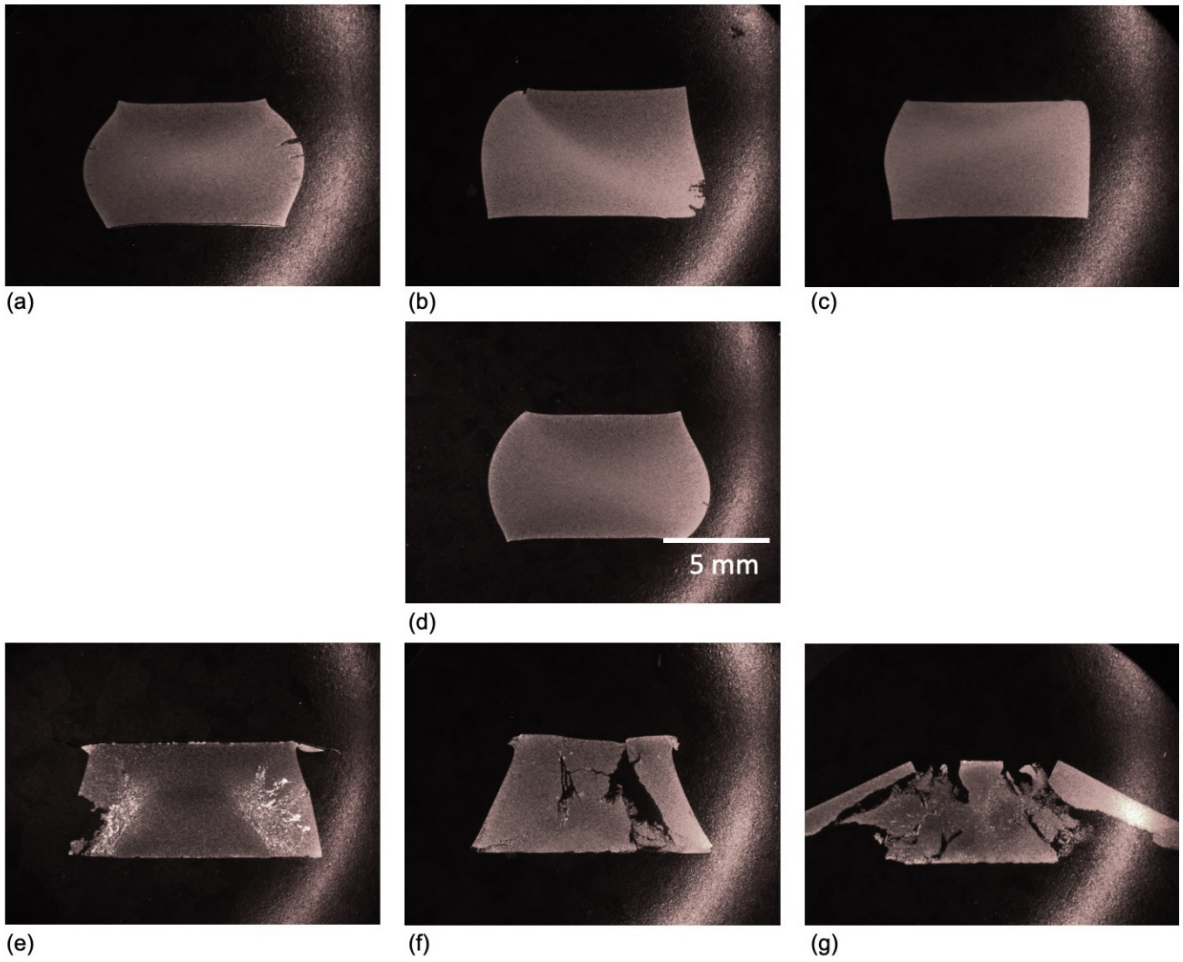

Figure 7.—Optical macro-images of longitudinal specimen sections for LSHR after: (a) 1010 °C-0.01 s^{-1}, (b) 1010 °C-1 s^{-1}, (c) 1010 °C-10 s^{-1}, (d) 1093 °C-0.1 s^{-1}, (e) 1177 °C-0.01 s^{-1}, (f) 1177 °C-1 s^{-1}, (g) 1177 °C-10 s^{-1}. The loading direction is vertical. Substantial cracking occurred for deformation at 1177 °C.

the latter specimens are shown in Figure 9. Here, different colors represent the different crystallographic orientation of each grain, making it easier to discern different grains. The three images showing specimens tested at 1177 °C have the “Image Quality” map overlaid to show where cracks are. These specimens tested at 1177 °C had equiaxed grains without smaller grains at the grain boundaries, (as seen in Figure 8(a) to (d), indicating full recrystallization had occurred.

Optical and SEM images of features noted in specimens tested near 1010 and 1177 °C are shown in Figure 10 and Figure 11. Cavities were often observed at the triple points of grain boundaries near cracks for specimens tested at all temperatures. These cavities were sometimes connected by cracks along the grain boundaries. The measured flow instabilities in tests at these temperatures appeared to coincide with dynamic recrystallization near 1177 °C, which is known to result in flow softening (Ref. 18) and failures attributed to adiabatic shear (Refs. 19 to 21). In the present study, the flow softening was intensified by extensive cavitation at the new grain boundaries. It could be that the peak stress in these curves may coincide with the point where the flow softening from rapid dynamic recrystallization overwhelms the inherent strength of the pre-existing microstructure. It would be difficult to interrupt additional tests near the peak stress and before failure in these unstable flow conditions, yet such tests could be useful for exploring this possible explanation.

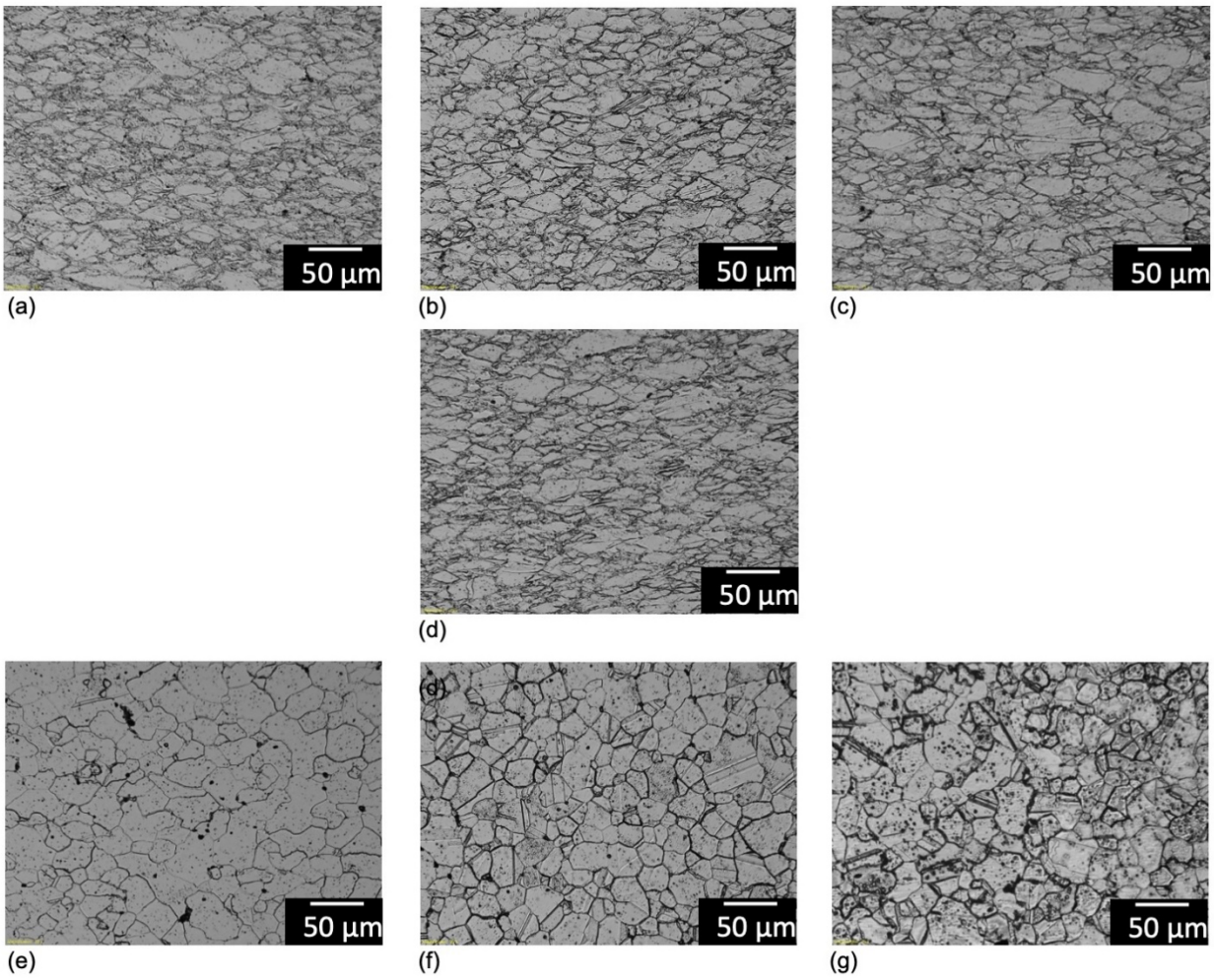

Figure 8.—Optical images of grain microstructures at the center of each cross section for LSHR after: (a) 1010 °C-0.01 s^{-1}, (b) 1010 °C-1 s^{-1}, (c) 1010 °C-10 s^{-1}, (d) 1093 °C-0.1 s^{-1}, (e) 1177 °C-0.01 s^{-1}, (f) 1177 °C-1 s^{-1}, (g) 1177 °C-10 s^{-1}. The loading direction is vertical. Recrystallized, equiaxed grains predominated for deformation at 1177 °C.

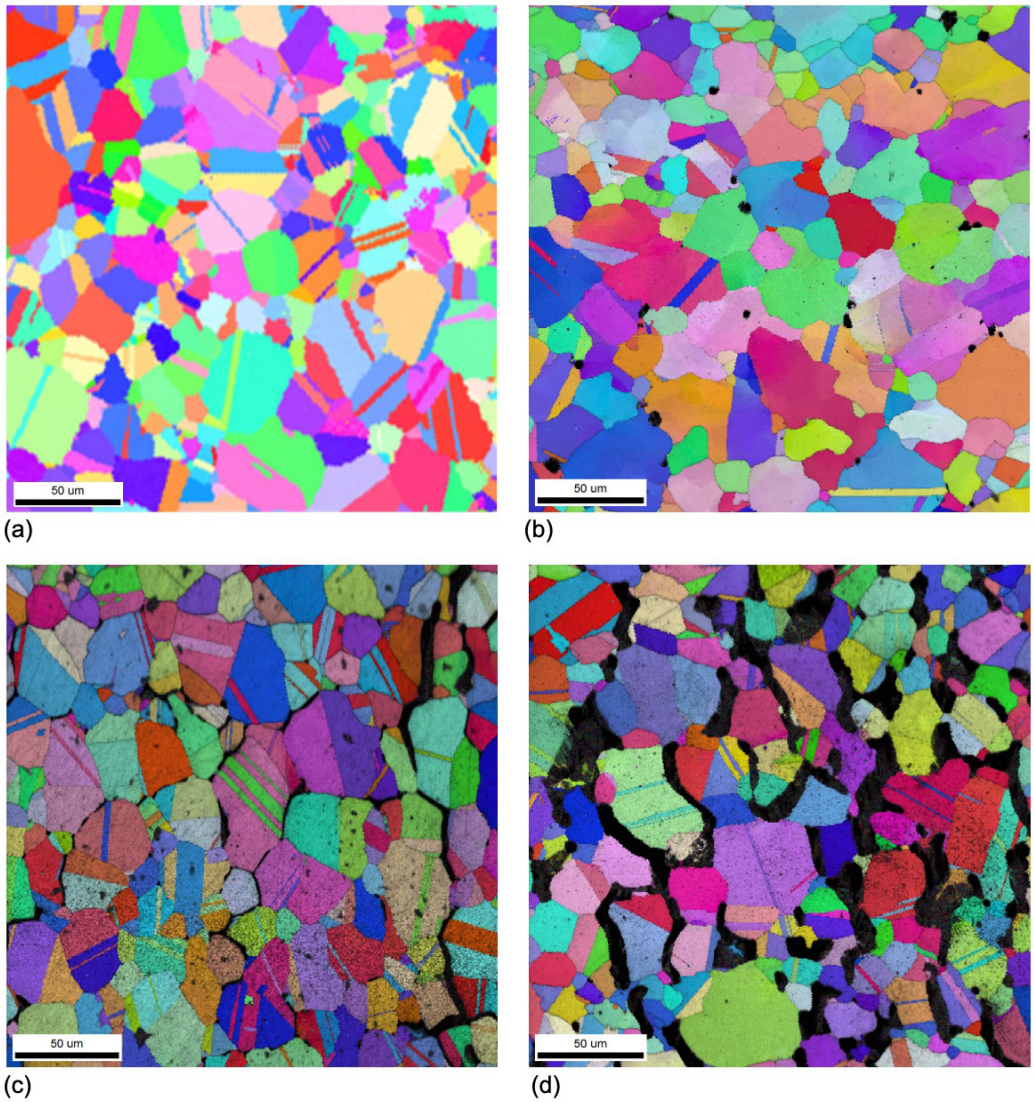

Figure 9.—EBSD IPF maps of (a) representative LSHR microstructure (b) tested at 1177 °C, 0.01 s^{-1} (c) tested at 1177 °C, 1 s^{-1} (d) tested at 1177 °C, 10 s^{-1}. The loading direction is vertical.

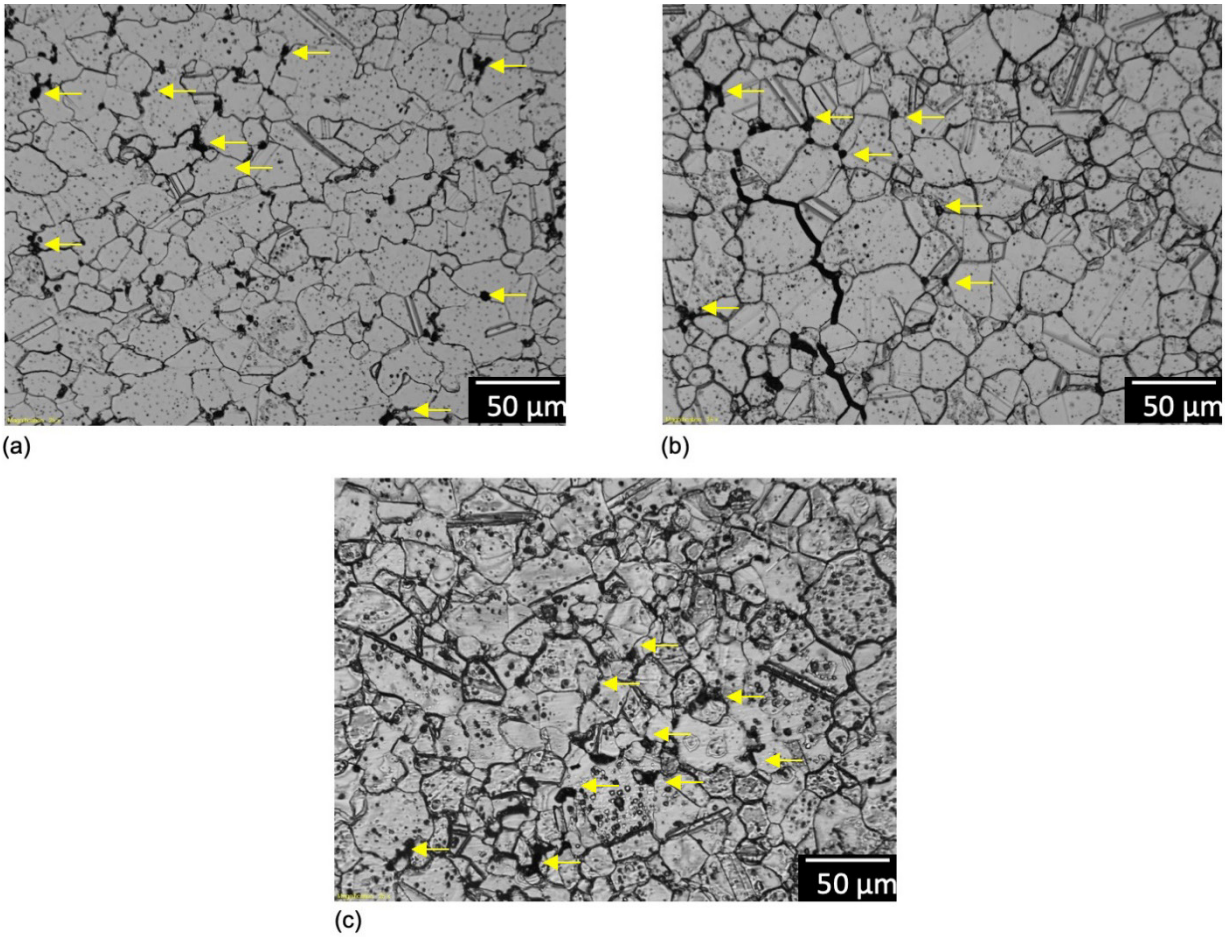

Figure 10.—Optical images of many cavities growing at grain boundaries for LSHR after deformation at: a. 1177 °C-0.01 s^{-1}, (b) 1177 °C-1 s^{-1}, (c) 1177 °C-10 s^{-1}. The arrows indicate cavities, which were sometimes connected by intergranular cracks.

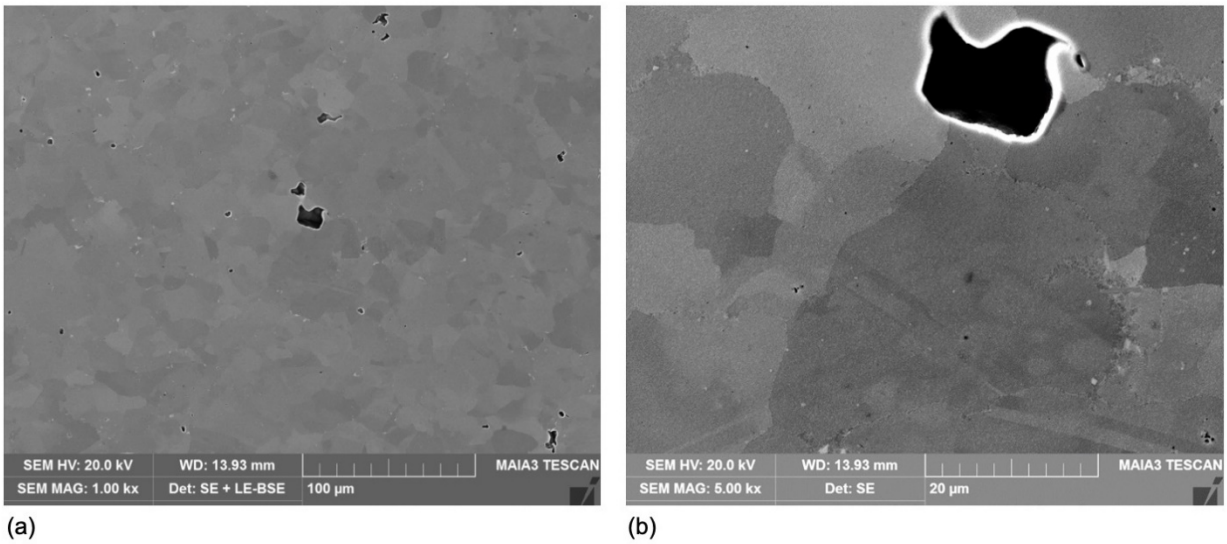

Figure 11.—Scanning electron microscope images acquired using (a) both the SE and BSE detectors, and (b) acquired using the SEL detector showing cavitation at grain boundaries of LSHR tested at 1177 °C-0.1 s^{-1}. The loading direction is vertical.

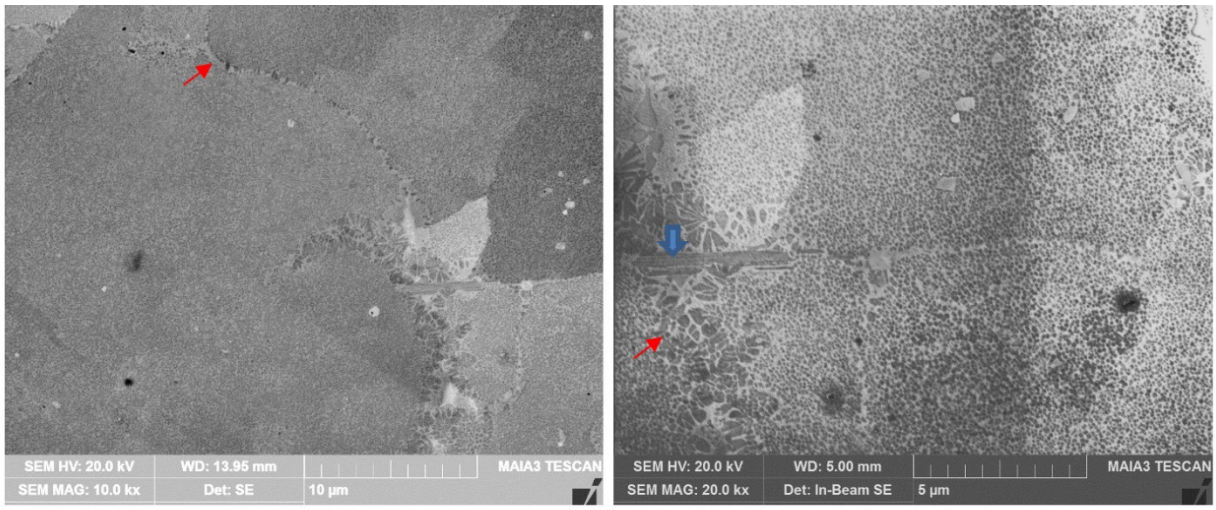

Figure 12.—Scanning electron microscope SE images showing phase instabilities at grain boundaries of LSHR after 1177 °C-0.1 s^{-1}. An elongated phase (blue arrow) and cellular γ‘ (red arrow) were observed at scattered grain boundaries near the outer periphery of the specimen. The loading direction is vertical.

There were also phase instabilities noted at scattered grain boundaries near the periphery of specimens tested at 1177 °C as shown in Figure 12, including the formation of cellular γ′ structures and different, elongated phases believed to be μ or σ which can form at lower temperatures in this superalloy (Ref. 22). Since the test temperature of 1177 °C is above the solvus temperature of the γ′ phase (Refs. 4 and 15), the cellular γ′ structures here were presumed to form during cooling after the compression test was completed. As the solution temperatures of both μ and σ phases are below the compression testing temperatures (Ref. 22), these apparently also formed during cooling after the test was completed. For these reasons, both phase instabilities were not characterized in detail for this study of compression responses at temperatures where the above phases were not believed to be present.

Images of the failure modes observed in fractured regions of test specimens run at hot, fast unstable conditions are compared in Figure 13. Fully intergranular failures were observed for the baseline coarse grain condition as well as the two fine grain conditions.

Single Crystal Compression Response

Stress-Strain Response

True stress-strain curves are shown for all tests of SC-180 in Figure 14. True stress-strain curves generated for solution heat treated SC-180 are shown in Figure 14(a). Stress at a given strain clearly increased with increasing strain rate and decreasing temperature. Surprisingly, at the minimum test temperature of 1010 °C, specimens often completed separated into two pieces by shear failure before reaching a true strain of 0.70.

The unstable response observed for the solution heat treated SC-180 in tests near 1010 °C could be related to the relatively wide range of secondary γ′ precipitate sizes observed for this heat treatment condition. To further explore this unstable response, additional specimens with the full solution and aging heat treatments giving more uniform γ′ precipitate sizes, shown in Figure 3, were also tested at all baseline conditions. The resulting stress-strain curves for fully heat treated SC-180 are shown in Figure 14(b). The fully heat treated specimens still had less ductile stress strain curves in tests at 1010 °C, and failed before reaching 0.70 mm/mm true strain. Compressive strength was modestly increased for

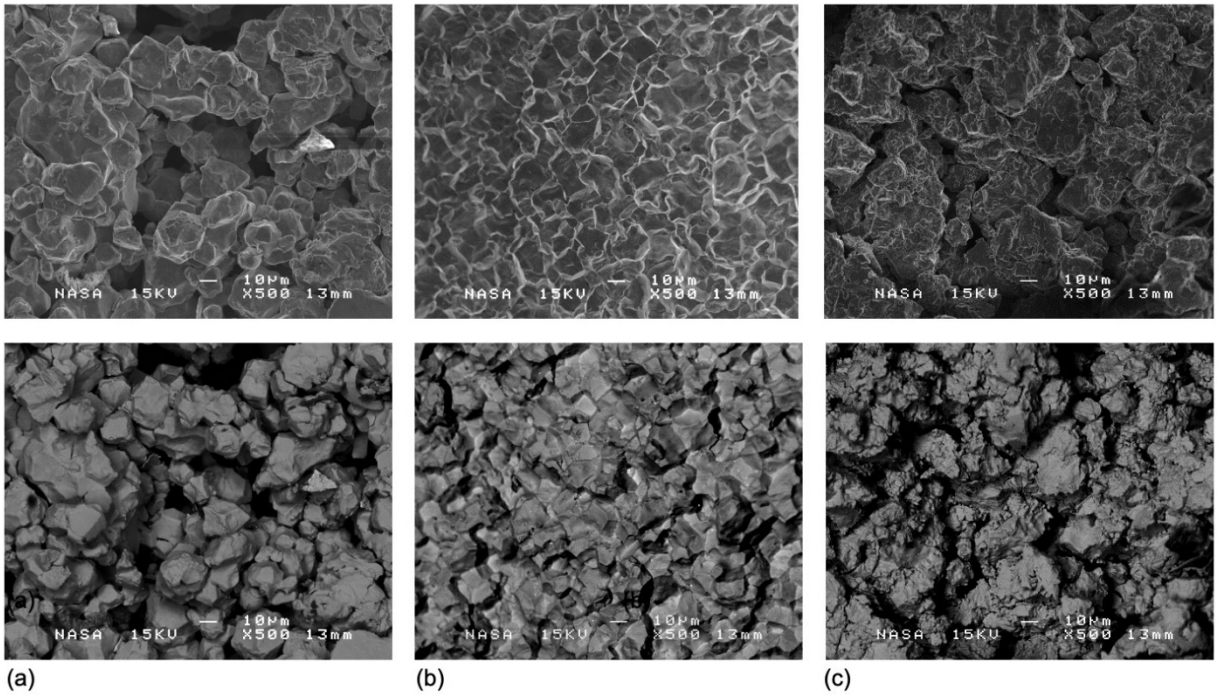

Figure 13.—SEM secondary electron images (upper) backscattered electron images (lower) of fractured areas in longitudinal sections of LSHR after compression testing at 1077 °C-3 s^{-1}: (a) coarse grain heat treatment, (b) fine grain heat treatment, (c) fine grain water quenched heat treatment. Intergranular failure predominated for all these heat treatment states.

some test conditions over that of the baseline solution heat treated specimens. In addition, the test at a temperature of 1096 °C now also displayed an unstable stress-strain response. Therefore, the full heat treatment with refined γ′ precipitate sizes did not improve the flow response of SC-180, but extended the temperature range of this unstable response to cover 1010 to 1094 °C.

The maximum stress generated during each test was again selected for comparisons of stress with respect to heat treatment condition, strain rate, and temperature. Plots of maximum stress versus temperature and versus strain rate are shown in Figure 15(a) and (b). Variations in maximum stress are evident for each heat treatment condition with temperature and strain rate. Here, the maximum stress was modestly higher for fully heat treated over as-solution heat treated SC-180. While a clear trend of stress versus temperature is apparent for each condition, additional variations in stress due to strain rate are also clearly evident.

The strain rate sensitivity m was evaluated by again fitting linear regression equations to the log(Max stress) data as a function of log(strain rate) at constant temperature. The log(Max stress) responses of SC-180 versus log(strain rate) are shown in Figure 16. Higher strain rate sensitivity was observed for tests at 1177 °C than those at 1010 °C. Heat treatment condition did not have a large or consistent effect on strain rate sensitivity. Instead, the strain rate sensitivity m was below 0.1 for all these test conditions, and hence SC-180 in both heat treat conditions did not display a true superplastic response. Yet, the stable flow to a high true strain of 0.7 mm/mm observed at the highest temperature of 1177 °C suggested thermo-mechanical processes involving compression of sections in the <001> crystallographic directions could be viable in these conditions.

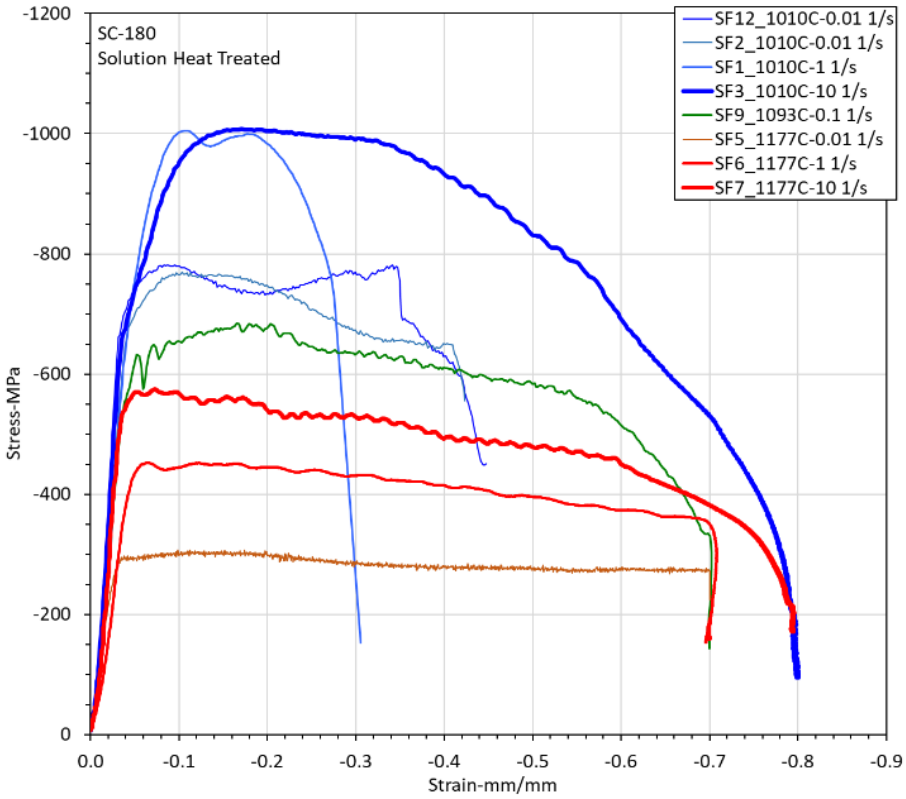

(a)

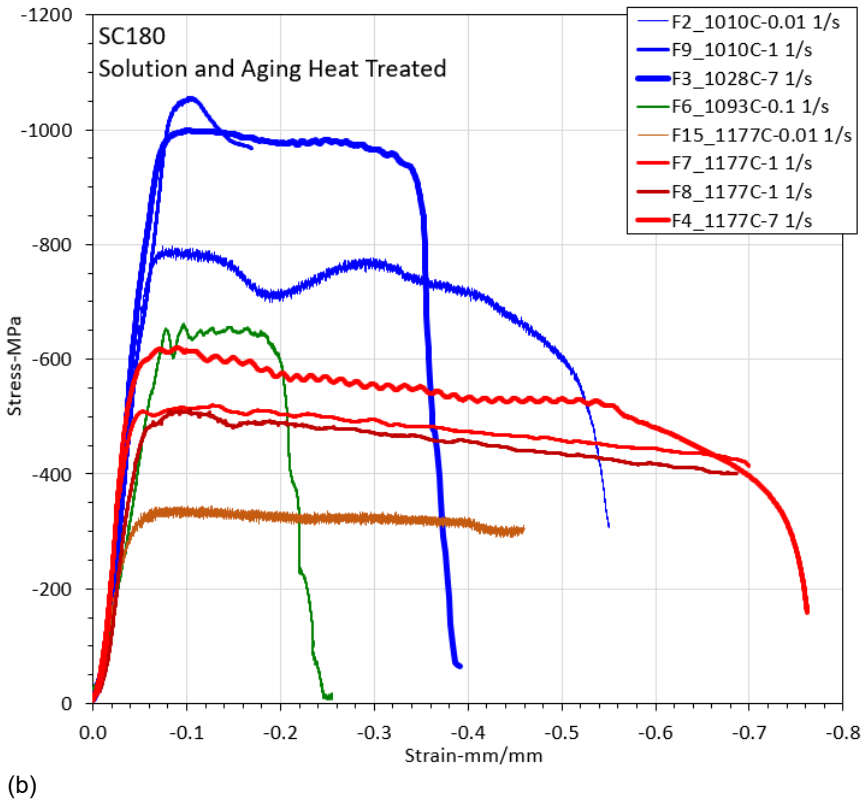

(b)

Figure 14.—SC-180 true stress-true strain response after: (a) initial solution heat treatment, (b) subsequent solution and aging heat treatments.

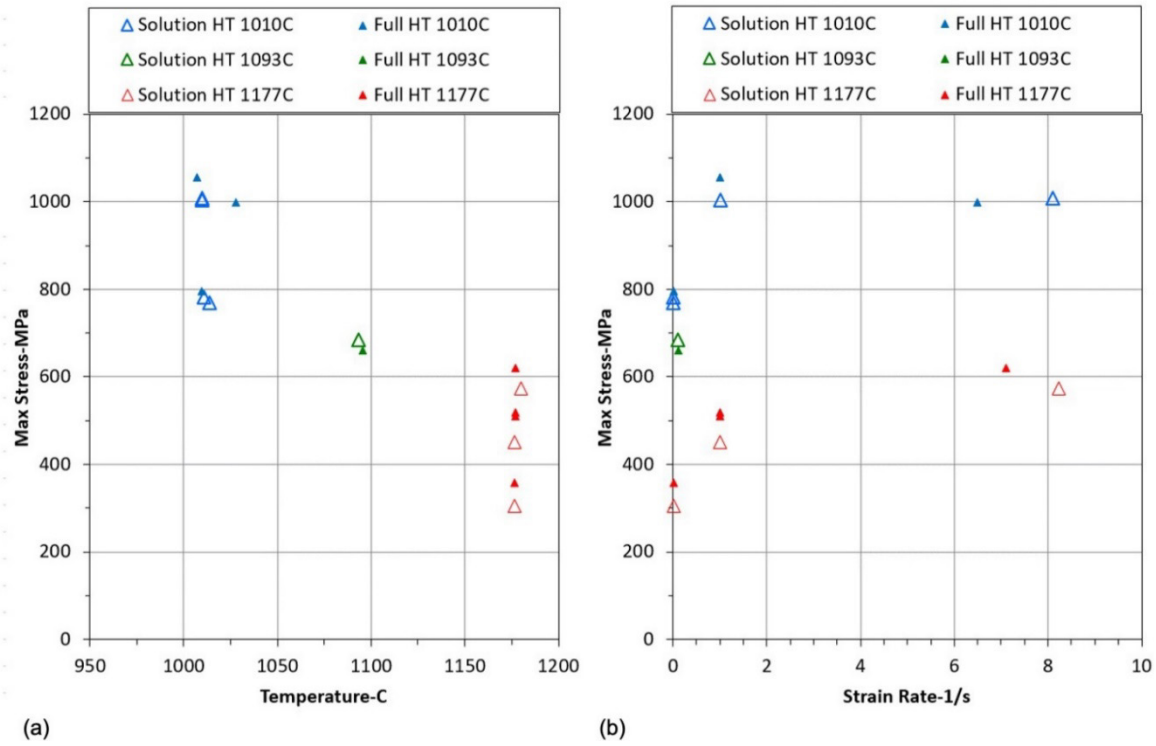

Figure 15.—Maximum stress response of SC-180 versus: (a) temperature and (b) strain rate for solution heat treated material shown in open symbols and fully heat treated material shown in filled symbols.

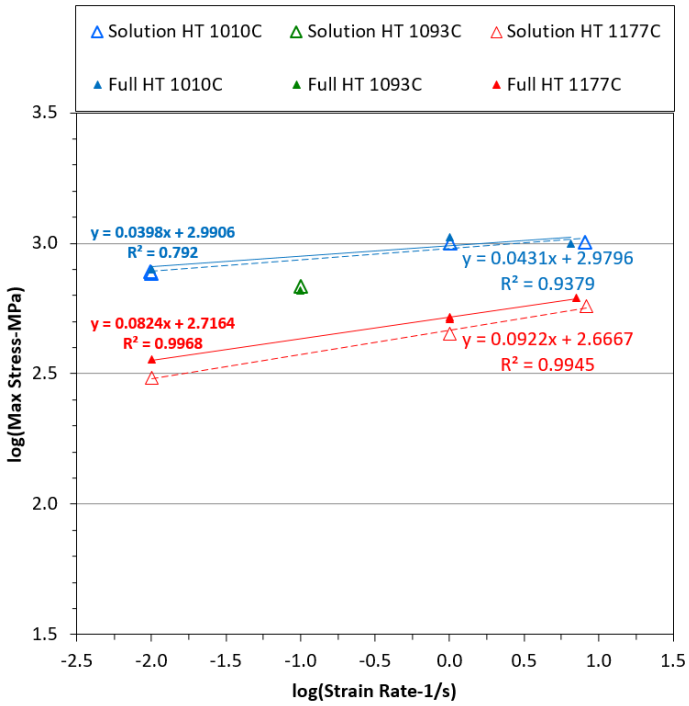

Figure 16.—Log(Maximum stress) versus log(strain rate) response of SC-180 for solution heat treated material shown in open symbols and fully heat treated material shown in filled symbols. The low slopes of the regressed lines indicate low strain rate sensitivities m at 1010 °C (blue lines) and 1177 °C (red lines).

The dependencies of maximum compressive stress on temperature and strain rate were generally consistent with several studies of tensile yield strength versus strain rate on single crystal superalloy PWA 1480 (Refs. 23 and 24). The unstable response that occurred in the present tests at the lowest test temperature near 1010 °C for various strain rates cannot be fully explained at this time. Other studies of failure modes in single crystal superalloys near this temperature have more usually reported cracking normal to the loading axis in tension (Refs. 25 and 26), while no relevant publications could be found describing their failure modes in compression near this temperature.

Deformation-Slip Relationships

Images of the deformed specimen cross sections observed for solution heat treated and fully heat treated SC-180 specimens after varied compression test conditions are compared in Figure 17 and Figure 18. The images are arranged in rows as isotherms in order to indicate changes with increasing compression test temperature and in columns of increasing strain rate. Severe cracking was observed in tests at the lowest temperature of 1010 °C. Only minor cracks were observed at the side surfaces of specimens deformed at the highest temperatures. Fully heat treated SC-180 specimens displayed the same trends.

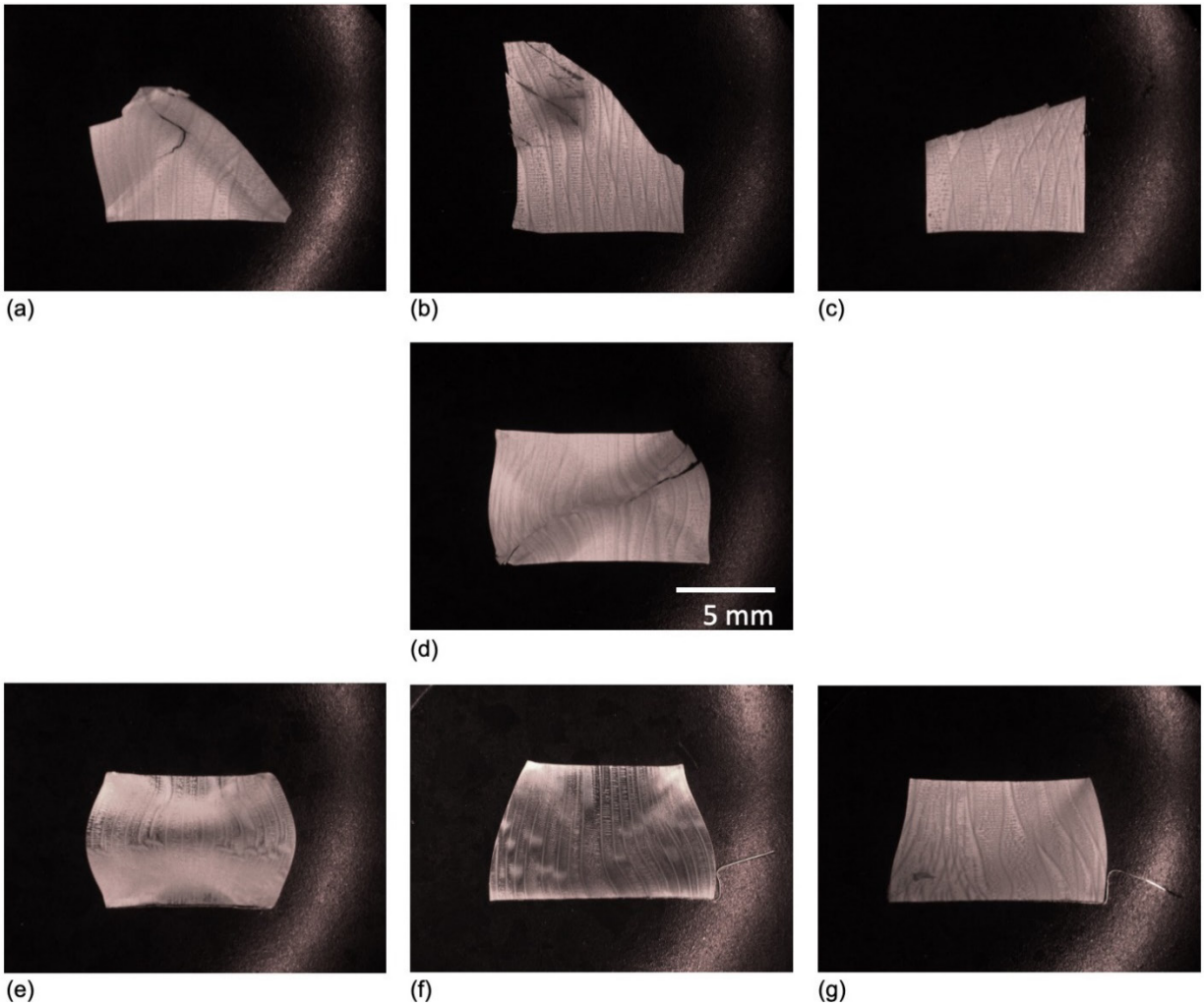

Figure 17.—Optical images of longitudinal specimen sections for solution heat treated SC-180 after: (a) 1010 °C-0.01 s^{-1} , (b) 1010 °C-1.0 s^{-1}, (c) 1010 °C-10 s^{-1}, (d) 1093 °C-0.1 s^{-1}, (e) 1177 °C-0.01 s^{-1}, (f) 1177 °C-1 s^{-1}, (g) 1177 °C-10 s^{-1} the loading direction is vertical. Cracking occurred along slip bands during unstable deformation near 1010 °C.

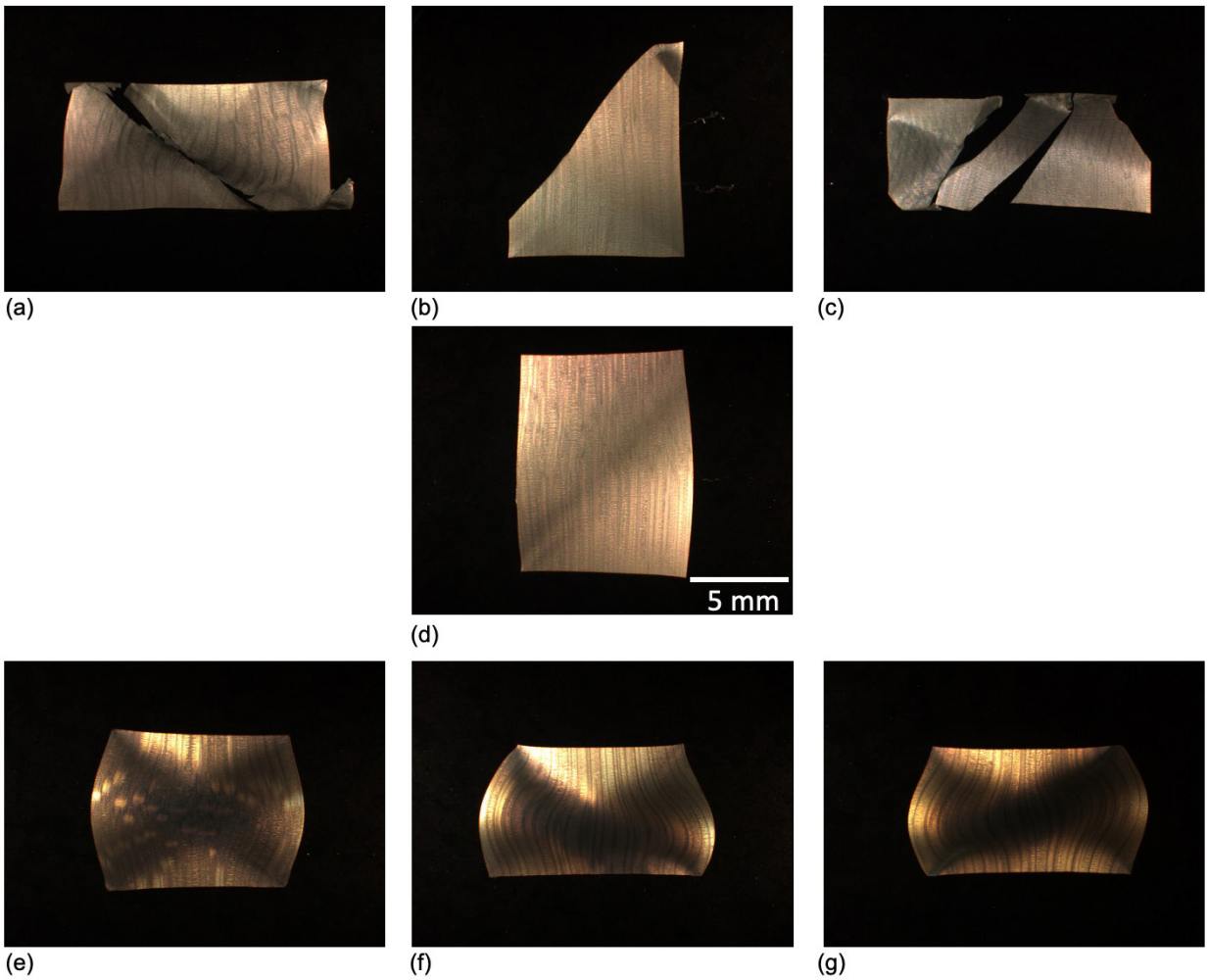

Figure 18.—Optical images of longitudinal specimen sections for fully heat treated SC-180 after: (a) 1010 °C-0.01 s^{-1}, (b) 1010 °C-1.0 s^{-1}, (c) 1010 °C-10 s^{-1}, (d) 1093 °C-0.1 s^{-1}, (e) 1177 °C-0.01 s^{-1}, (f) 1177 °C-1 s^{-1}, (g) 1177 °C-10 s^{-1} the loading direction is vertical. Cracking occurred along slip bands during unstable deformation near 1010 °C.

Images at higher magnifications from longitudinal metallographic sections prepared from selected SC-180 specimens are compared in Figure 19 and Figure 20. Slip bands sometimes accompanied by shear cracks were observed in as-solutioned and fully heat treated SC-180 specimens tested at 1010 °C, but not at higher temperatures. Images at higher magnification showing the slip bands from SC-180 specimens tested at 1010 °C are shown in Figure 20. It appeared that very fine recrystallized grains could be present within the slip bands. However, these features were too fine to confirm at the present time that these were recrystallized grains. Very similar features that were confirmed to be recrystallized grains have been observed, accompanied by preferential cracking, in specimens of CMSX-4 subjected to thermo-mechanical fatigue cycles extending up to 1000 °C (Ref. 27). This suggests that these features observed in the present study could help explain the unstable compression response of SC-180 at 1010 to 1094 °C.

Typical fracture surfaces produced in shear failures during several tests at 1010 °C are shown in Figure 21. The planar failures occurred along slip bands, visible on the specimen sides adjacent to the failures. Such planar crystallographic fracture modes have been reported for numerous single crystal superalloys after tensile and fatigue loading at lower temperatures (Refs. 25 to 27). However, reports of slip plane failures in monotonic compression at the present conditions were not found in the published literature.

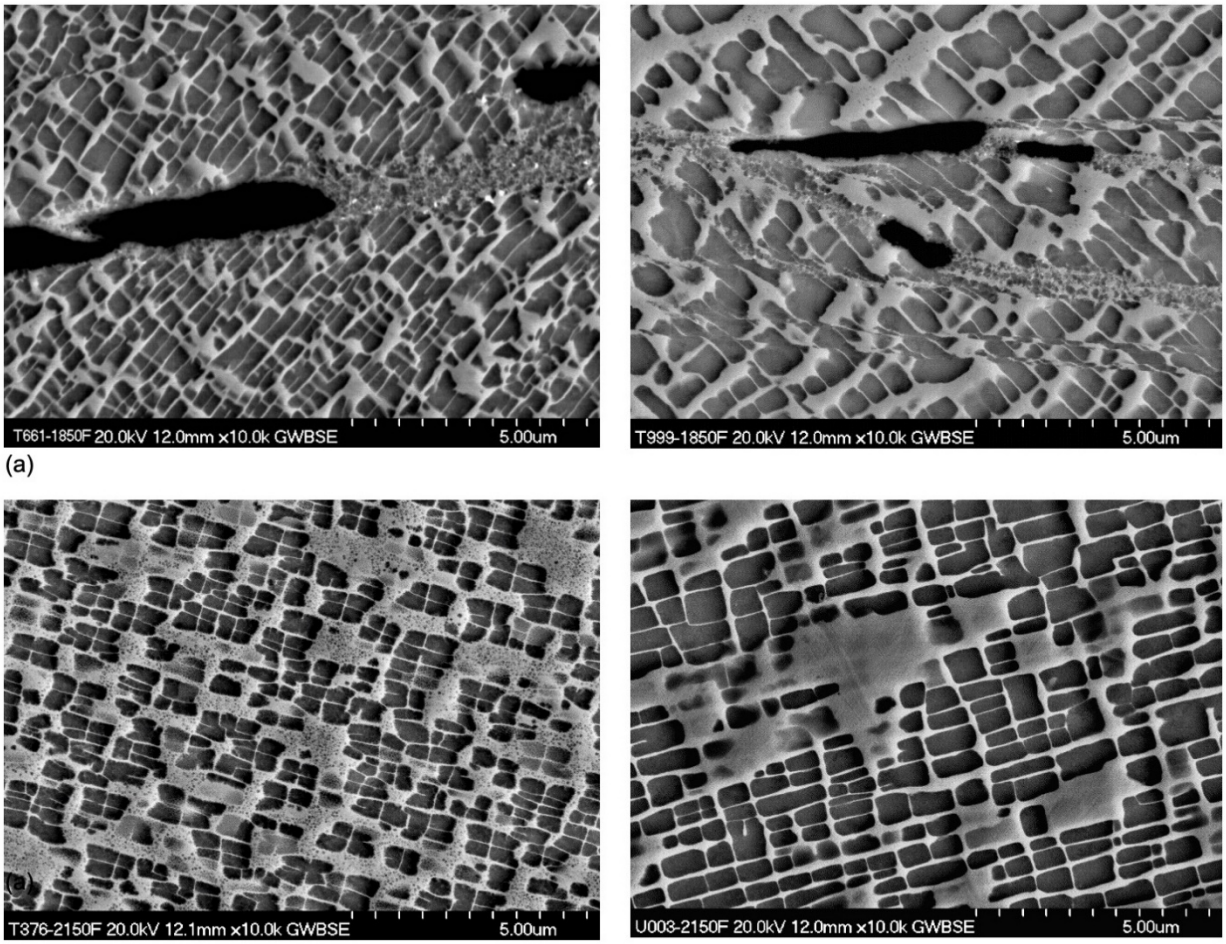

Figure 19.—Scanning electron microscope BSE images of deformed microstructure at the center of each cross section for solution heat treated (left) versus fully heat treated (right) SC-180 after testing at (a) 1010 °C-1 s^{-1}, (b) 1177 °C-1 s^{-1}.

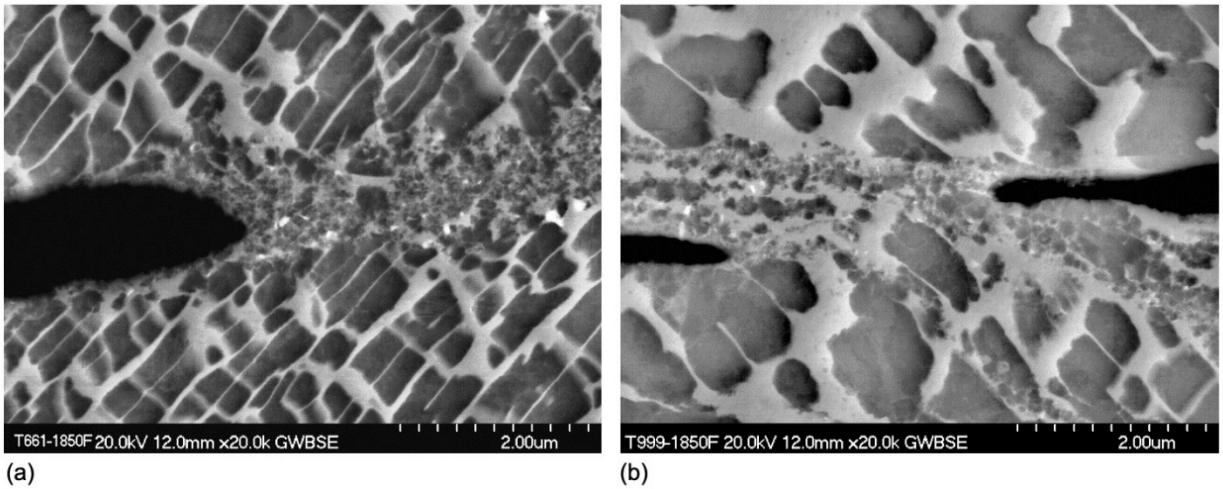

Figure 20.—Scanning electron microscope BSE images of slip bands near the center of each cross section after testing at 1010 °C-1 s^{-1} of (a) solution heat treated (left) versus (b) fully heat treated (right) SC-180.

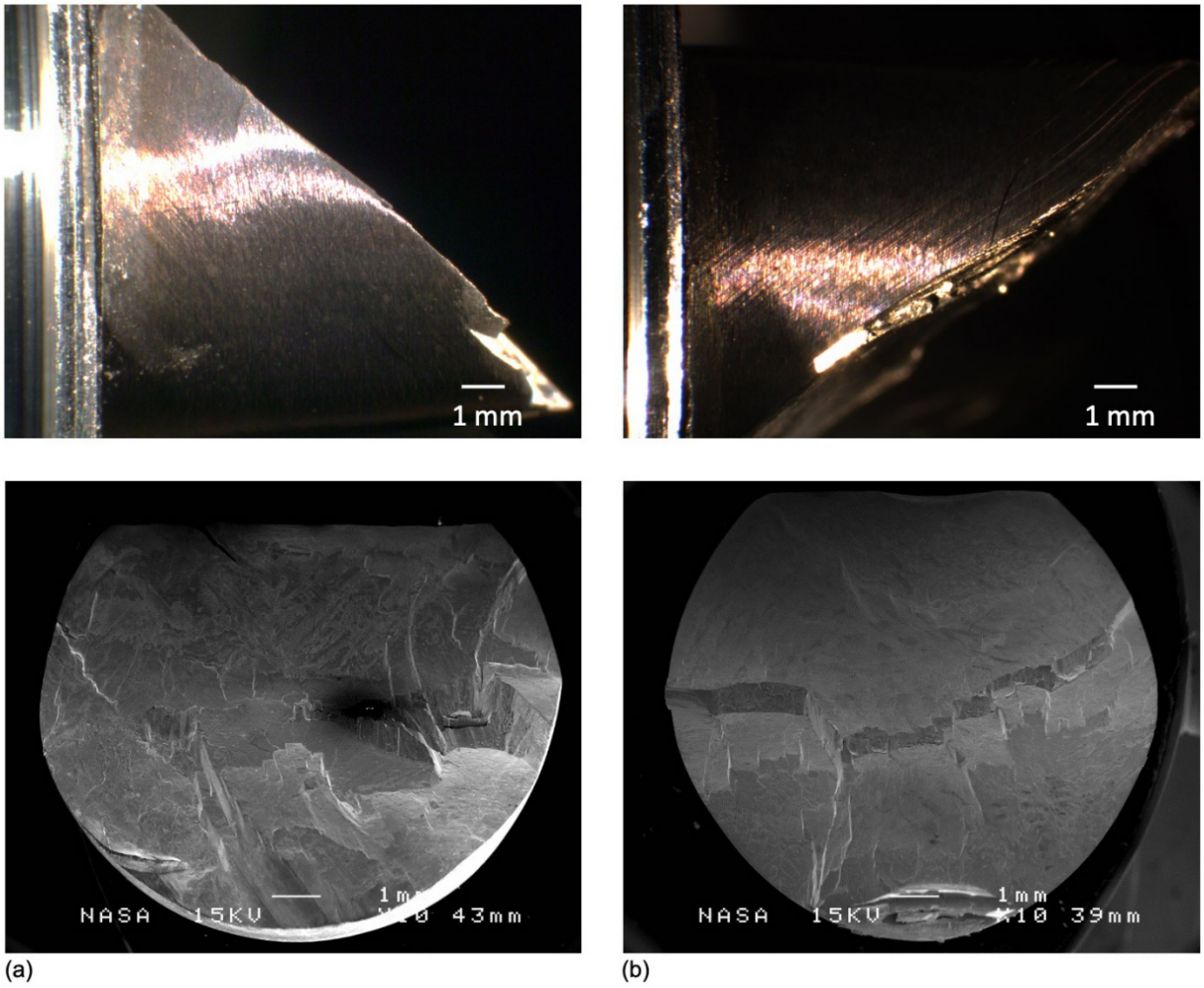

Figure 21.—Optical and scanning electron microscope SE images of fracture surfaces from (a) solution heat treated versus (b) fully heat treated SC-180 after testing at 1010 °C-1 s^{-1}.

Comparisons of LSHR and SC-180 Compression Stress-Strain Responses

Maximum stress was used for comparison of compression responses between the two alloys. In order to consistently compare the effects of changing temperature and strain rate on maximum stress generated between the two alloys, forward and reverse stepwise selection linear regressions of the common logarithm of maximum stress were performed separately for each alloy, using the same variables standardized as described in equation 1: temperature (T'), the common logarithm of the strain rate (($log(d\varepsilon/dt)'$), and their interactive product. The resulting linear regression equations were:

$$\text{Coarse grain LSHR: } \log(\text{Max. stress}) = 2.3978 - 0.4875\ T' + 0.2413\ log(d\varepsilon/dt)' \tag{3}$$

with an adjusted coefficient of determination $R^2_{adj} = 0.93$ and rms error = 0.1149.

$$\text{Solution heat treated SC-180: } \log(\text{Max. stress}) = 2.7997 - 0.1735\ T' + 0.0963\ log(d\varepsilon/dt)' + 0.0381\ T'\ log(d\varepsilon/dt)' \tag{4}$$

with an adjusted coefficient of determination $R^2_{adj} = 0.95$ and rms error = 0.0393.

$$\text{Fully heat treated SC-180: } \log(\text{Max. stress}) = 2.8296 - 0.1572\,T' + 0.0947\,\log(d\varepsilon/dt)' + 0.0260\,T'\,\log(d\varepsilon/dt)' \quad (5)$$

with an adjusted coefficient of determination $R^2_{adj} = 0.98$ and rms error = 0.0190.

Plots of actual maximum stress versus that estimated by these equations are shown in Figure 22 for LSHR and SC-180, which indicate satisfactory agreement.

In these regression equations, the greater magnitude of the coefficient for temperature than the coefficient for log(strain rate) with each alloy reflected that temperature over its range of variation had a stronger influence in reducing maximum stress than did log(strain rate) over its range of variation in these tests. The greater magnitudes of the coefficients for temperature and log(strain rate) for LSHR than for SC-180 reflected that maximum stress in LSHR was more strongly affected by these variables than for SC-180 over the range of tested conditions. This can be attributed to the presence of grain boundaries in LSHR, where grain boundary sliding can allow more enhanced flow with increased temperatures than for SC-180. The interaction product of the temperature (T') and the common logarithm of the strain rate (($\log(d\varepsilon/dt)'$), was found to be statistically significant in both solution heat treated and fully heat treated SC-180. This term in the equations indicates that maximum stress was enhanced for SC-180 by combinations of high temperature and high strain rate. This interaction term did not have a significant effect on maximum stress for LSHR.

Deformation-Heating Relationships

Adiabatic heating during compression testing at high temperatures has been reported in compression tests of many polycrystalline superalloys (Ref. 20). This heating is generally encountered at high temperatures and high strain rates (Ref. 28). In the present tests, such dynamic heating was usually compensated for by the direct resistance heating system employed, through a closed-loop control system which maintained the temperature of the spot-welded thermocouple at mid-gage. Consequently, no consistent dynamic temperature increase was recorded between the start of the test and the instant of attaining peak stress in the compression tests of LSHR. However, this was not always the case in tests of SC-180. The measured dynamic temperature increase between the start of the test and the instant of attaining maximum stress is shown versus strain rate and starting test temperature for all tests of SC-180 in Figure 23. A significant dynamic temperature increase was apparent in tests of SC-180, maximized in tests at 1010 °C performed with a strain rate of 10 s^{-1}. These dynamic temperature increases were highest for fully heat treated SC-180.

To test the statistical significance of this observation, forward and reverse stepwise selection linear regressions of the dynamic temperature rise from the start of the test to attainment of maximum compressive stress were performed separately for LSHR, solution heat treated SC-180, and fully heated SC-180, using the same standardized variables of temperature (T′), log(strain rate) ($\log(d\varepsilon/dt)'$), and their interactive product. No significant relationships could be derived for LSHR. However, for SC-180 significant linear regression relationships were present:

$$\text{Solution heat treated SC-180: Temperature Increase} = 6.9 - 3.4\,T' + 9.2\,\log(d\varepsilon/dt)' - 4.7\,T'\,\log(d\varepsilon/dt)' \quad (6)$$

with an adjusted coefficient of determination $R^2_{adj} = 0.95$ and rms error = 3.0.

$$\text{Fully heat treated SC-180: Temperature Increase} = 13.8 - 10.2\,T' + 13.8\,\log(d\varepsilon/dt)' - 14.5\,T'\,\log(d\varepsilon/dt)' \quad (7)$$

with an adjusted coefficient of determination $R^2_{adj} = 0.82$ and rms error = 7.6.

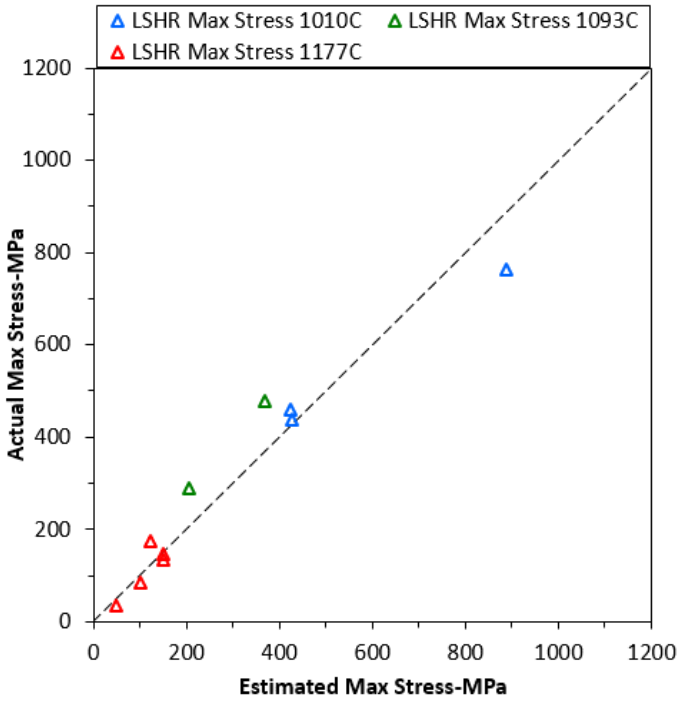

(a)

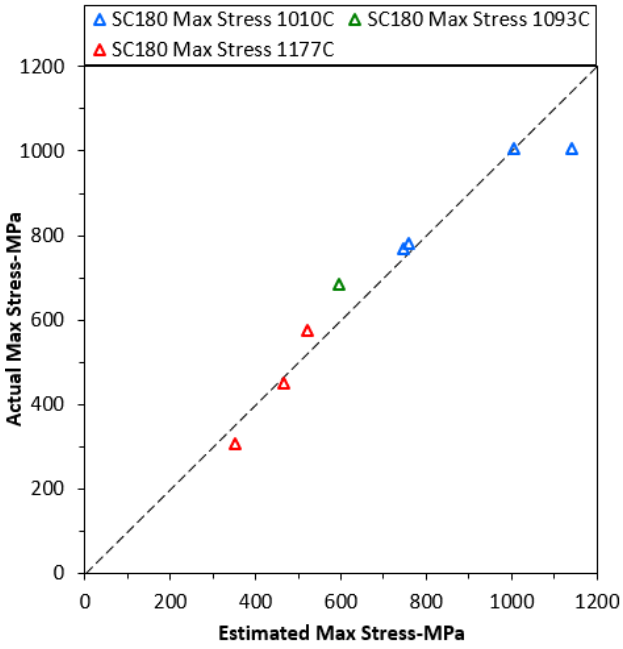

(b)

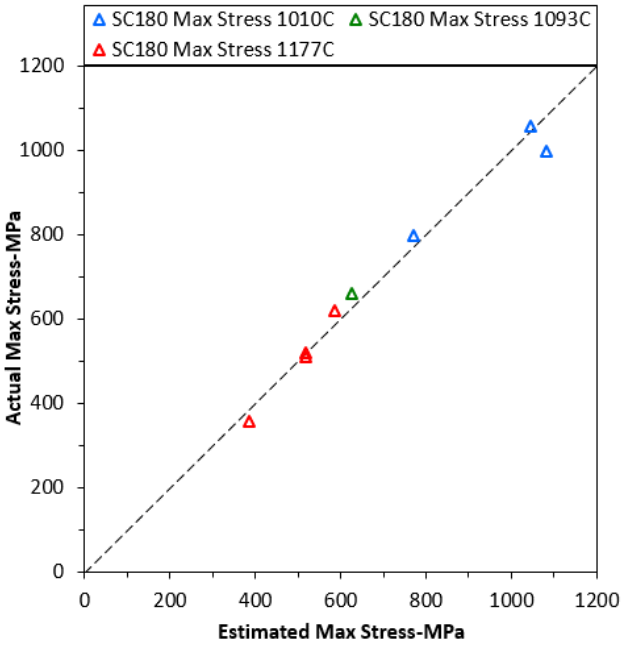

(c)

Figure 22.—Comparisons for agreement of estimated versus actual maximum compressive stress values using the regressed Equations (3), (4), and (5) with standardized variables T' and $log(R)'$ for (a) coarse grain LSHR, (b) solution heat treated SC-180, and (c) fully heat treated SC-180. The dashed lines represent perfect agreement.

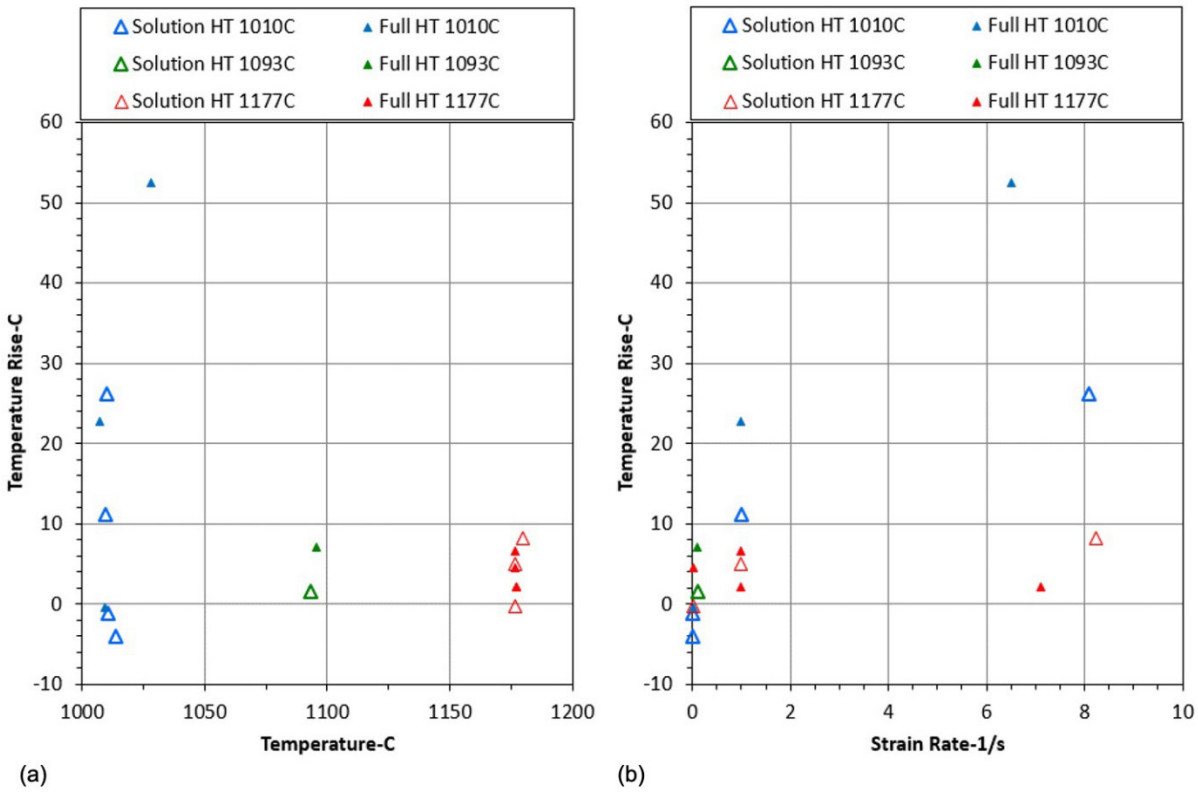

Figure 23.—Temperature rise from the start of the test to attainment of maximum stress versus (a) test temperature, and (b) strain rate for SC-180. Significant temperature rises occurred for tests at 1010 °C and high strain rates in spite of the closed-loop temperature control system.

The relationships indicated that the dynamic temperature increase was correlated with increasing strain rate, decreasing test temperature, and enhanced for combinations of low temperature and high strain rates. Comparison of the relationships indicated the temperature increase was enhanced for fully heat treated SC-180 over that of solution heat treated SC-180. These results suggest there were higher rates of adiabatic heating during compressive loading of single crystal SC-180 than for polycrystalline LSHR in these conditions, which the temperature control system could not fully compensate for. Additional testing would be necessary to fully confirm and evaluate this effect, perhaps with the closed-loop temperature control temporarily suspended during compressive loading. However, other factors could also be influencing the observed temperature increases. For example, this heating control system could have been influenced by interactions between the temperature control and inhomogeneous slip events during tests of SC-180, as evident in the inhomogeneous slip bands of cross sections presented in Figure 19 and Figure 20.

Summary and Conclusions

1. Polycrystalline disk superalloy LSHR and single crystal blade superalloy SC-180 can allow substantial stable compressive deformation at maximum stresses that vary with strain rate, when combined with suitable test temperatures.
2. A test temperature near 1177 °C could be suitable for stable compressive deformation of SC-180, but lower temperatures of 1010 to 1093 °C are necessary for stable compressive flow of LSHR.

3. This could allow thermo-mechanical processes such as hot pressing and forging to be applied to both the polycrystalline and single crystal superalloys for certain applications, provided suitable process controls and die materials can be utilized at their suitable temperatures and strain rates.
4. Both superalloys give unstable response and failure in other compression test conditions, occurring at lower test temperatures for SC-180 than for LSHR.
5. Unstable compression response of LSHR is associated with dynamic recrystallization at the highest test temperature, allowing void formation and cracking to occur at grain boundaries.
6. Unstable compression response in SC-180 is associated with slip concentrated in deformation bands at lower test temperatures, promoting shear failures.

References

1. C.S. Sims, N.S. Stoloff, W.C. Hagel, ed. Superalloys II, John Wiley and Sons, New York, NY, 1987, pp. 459–492.
2. R.C. Reed, The Superalloys, Cambridge University Press, Cambridge, UK, 2006, pp. 217–252.
3. R.G. Menzies, J.W. Edington, G.J. Davies "Superplastic Behavior of Powder-consolidated Nickel-base Superalloy IN-100", Metal Science, V. 15(5), 1981, pp. 210–216.
4. S.L. Semiatin, K.E. McClary, A.D. Rollett, C.R. Roberts, E.J. Payton, F. Zhang, T.P. Gabb, "Plastic Flow and Microstructure Evolution During Thermomechanical Processing of a PM Nickel-Base Superalloy," Met. Trans. A, V. 44A(6), 2013, pp. 2778–2013.
5. R.G. Menzies, G.J. Davies, J.W. Edington, "Microstructural Changes During Recrystallization of Powder-consolidated Nickel-base Superalloy IN-100", Metal Science, V. 15(5), 1981, pp. 217–224.
6. S.L. Semiatin, J.M. Shank, A.R. Shiveley, W.M. Saurber, E.F. Gaussa, A.L. Pilchak, "The Effect of Forging Variables on the Supersolvus Heat-Treatment Response of Powder-Metallurgy Nickel-Base Superalloys," Met.Trans. A, V. 45A, 2014, pp. 6231–6251.
7. G.R. Leverant, M. Gell, S.W. Hopkins, "The Effect of Strain Rate on the Flow Stress and Dislocation Behavior of a Precipitation-hardened Nickel-base Alloy," Materials Science and Engineering, V. 8 (3), 1971, pp. 125–133.
8. R.V. Miner, T.P. Gabb, J. Gayda, K.J. Hemker, "Orientation and Temperature Dependence of Some Mechanical Properties of the Single Crystal Nickel-Base Superalloy Rene' N4: Part III. Tension-Compression Anisotropy," Met. Trans. A, 1986, V. 17A, pp. 507–512.
9. T. Link, M. Feller-Kniepmeier, "Shear Mechanisms of the γ′ Phase in Single-crystal Superalloys and Their Relation to Creep," Met. Trans. A, 1992, V. 23, pp. 99–105.
10. T.M. Smith, R.R. Unocic, H. Deutchman, M.J. Mills, "Creep Deformation Mechanism Mapping in Nickel Base Disk Superalloys," Materials at High Temperatures, 2016, V. 33(4–5), pp. 372–383.
11. T.M. Smith, B.S. Good, T.P. Gabb, B.D. Esser, A.J. Egan, L.J. Evans, D.W. McComb, M.J. Mills, "Effect of Stacking Fault Segregation and Local Phase Transformations on Creep Strength in Ni-base Superalloys," Acta Materialia, V. 172, 2019, pp. 55–65.
12. M.F. Ashby, "A First Report on Deformation-Mechanism Maps," Acta Met., V. 20(7), 1972, pp. 887–897.
13. A. Lasalmonie, J.L. Strudel, "Interfacial Dislocation Networks Around γ′ Precipitates in Nickel-base Alloys," Phil. Mag., V. 32(5), 1975, pp. 937–949.
14. T.P. Gabb, R.A. MacKay, S.L. Draper, C.K. Sudbrack, M.V. Nathal, "The Mechanical Properties of Candidate Superalloys for a Hybrid Turbine Disk," NASA/TM—2013-217901, Washington, D.C., July, 2013.

15. X. Nguyen-Dinh, U.S. Patent 4,935,072, “Phase Stable Single Crystal Materials,” U.S. Patent Office, Wash. D.C., June 19, 1990.
16. P. Bereczki, B. Fekete, V. Szombathelyi, F. Misjak, “Different Applications of the Gleeble® Thermal–Mechanical Simulator in Material Testing, Technology Optimization, and Process Modeling,” Materials Performance and Characterization, V. 4(3), 2015, pp. 399–420.
17. B. Jones, J. Sall, “JMP Statistical Discovery Software,” WIREs Computational Statistics, V. 3(3), 2011, pp. 188–194.
18. G. Shen, D. Furrer, “Manufacturing of Aerospace Forgings,” Journal of Materials Processing Technology, V. 98(2), 2000, pp. 189–195.
19. M.C. Somani, K. Muraleedharan, Y.V.R.K. Prasad, V. Singh, “Mechanical Processing and Microstructural Control in Hot Working of Hot Isostatically Pressed PM IN-100 Superalloy,” Materials Science and Engineering A, V. 245, 1998, pp. 88–99.
20. S.S. S. Kumar, T. Raghu, P.P. Bhattacharjee, G.A. Rao, U. Borah, “Strain Rate Dependent Microstructural Evolution During Hot Deformation of a Hot Isostatically Processed Nickel Base Superalloy,” Journal of Alloys and Compounds, V. 681, 2016, pp. 28–42.
21. N. Srinivasa, Y.V.R.K. Prasad, “Hot Working Characteristics of Nimonic 75, 80A and 90 Superalloys: a Comparison Using Processing Maps,” J. Mat. Proc. Tech., V. 51(1–4), 1995, pp. 171–192.
22. T.P. Gabb, A. Garg, D.R. Miller, C.K. Sudbrack, D.R. Hull, D. Johnson, R.B. Rogers, J. Gayda, S.L. Semiatin, “Formation of Minor Phases in a Nickel-Based Disk Superalloy,” NASA/TM—2012-217604, Washington, DC, July 2012.
23. F.E. Heredia, D.P. Pope, “The Tension/Compression Flow Asymmetry in a High γ′ Volume Fraction Nickel Base Alloy,” Acta Met., V. 34(2), 1986, pp. 279–285.
24. M. Hebsur, R.V. Miner, “Elevated Temperature Tension, Compression, and Creep-Rupture Behavior of [001]-Oriented Single Crystal Superalloy PWA 1480,” NASA-TM-88950, Washington, D.C., 1987.
25. J.S. Crompton, J.W. Martin, “Crack Growth in a Single Crystal Superalloy at Elevated Temperature,” Met. Trans. A, V. 15(9), 1984, pp. 1711–1719.
26. J. Telesman, L.J. Ghosn, “Fatigue Crack Growth Behavior of PWA 1484 Single Crystal Superalloy at Elevated Temperatures,” J. Eng. Gas Turbines Power, V. 118, 1996, pp. 399–405.
27. J.J. Moverare, S. Johansson, R.C. Reed, “Deformation and Damage Mechanisms During Thermal–mechanical Fatigue of a Single-crystal Superalloy’, Acta Materialia, V. 57, 2009, pp. 2266–2276.
28. R.L. Goetz, S.L. Semiatin, “The Adiabatic Correction Factor for Deformation Heating During the Uniaxial Compression Test,” J. Mat. Eng. Perf., V. 10(6), 2001, pp. 710–717.